Recent Developments in the Theory of Scarring

L. Kaplan*
Department of Physics and Society of Fellows,
Harvard University, Cambridge, MA 02138

We review recent progress in attaining a quantitative understanding of the scarring phenomenon, the non-random behavior of quantum wavefunctions near unstable periodic orbits of a classically chaotic system. The wavepacket dynamics framework leads to predictions about statistical long-time and stationary properties of quantum systems with chaotic classical analogues. Many long-time quantum properties can be quantitatively understood using only short-time classical dynamics information; these include wavefunction intensity distributions, intensity correlations in phase space and correlations between wavefunctions, and distributions of decay rates and conductance peaks in weakly open systems. Strong deviations from random matrix theory are predicted and observed in the presence of short unstable periodic orbits.

I. INTRODUCTION

Wavefunction scarring is the anomalous enhancement of quantum eigenstate intensities along unstable periodic orbits of a classically chaotic system; it is surely one of the most visually striking properties of quantum chaotic behavior. Observed numerically in unpublished work by McDonald [1], scars were later brought to the attention of the physics community by Heller [2], who also provided the first theoretical explanation for their existence. Numerical evidence and associated analytical work (followed later by experimental tests in a variety of systems) showed that scarring was a statistically significant correction to Berry's early conjecture [3] that eigenstates of a classically ergodic system are evenly distributed over the energy hypersurface, in the semiclassical limit $\hbar \to 0$.

The structure of quantum eigenstates of a system whose classical analogue is ergodic has long been a matter of interest for physicists and mathematicians alike. When an integrable system is quantized, the resulting eigenstates can be well understood in terms of the WKB quantization condition along the classical periodic orbits [4]. For classically ergodic systems, such a direct correspondence between quantum wavefunctions and classical periodic orbits is, however, not possible. Because the typical classical trajectory evenly explores all of the available energy hypersurface, it is natural to suppose that the quantum eigenstates also have constant intensity over this entire hypersurface, up to the inevitable quantum fluctuations. Rigorous results have been obtained on one important aspect of this problem. Theorems by Schnirelman, Zelditch, and Colin de Verdiere [5] consider a classically defined operator and show that its expectation value over almost all individual eigenstates converges (in the semiclassical limit) to the ergodic, microcanonical average of the classical version of the operator. In this limit, however, taking the expectation value means averaging over more and more de Broglie wavelengths of the wavefunction, since the classical symbol of the operator in phase space is assumed to be kept fixed as $\hbar \to 0$. Thus, these ergodicity theorems provide little information about the structure of eigenstates at the single-wavelength scale (or more generally on scales of a single momentum-space channel or over cells of size $O(\hbar)$ in phase space).

Classical ergodicity by itself is certainly not sufficient to ensure ergodically distributed quantum wavefunctions over individual wavelengths or channels. Thus, for example, one can consider the "slow ergodic systems," [6] where the classical exploration of phase space is sufficiently slow that the corresponding quantum dynamics can only explore a fraction of the available quantum channels by the Heisenberg time [this being $\hbar$ over the mean quantum level spacing, the time at which the quantum exploration of phase space effectively ends and the quantum dynamics becomes quasi-periodic]. In such systems, the participation ratio, i.e. the fraction of available quantum channels with which a typical eigenstate has significant overlap, approaches zero in the semiclassical limit $\hbar \to 0$. However, for any given high-energy eigenstate, this small fraction of bright channels are evenly distributed over the total phase-space, so that eigenstate intensity integrated over a classically-defined patch of phase space does in fact converge to the classically required value, in perfect accordance with the results of Schnirelman, Zelditch, and Colin de Verdiere (SZCdV).

Such anomalies are not known to arise for strongly chaotic systems, by which we mean systems that have everywhere positive entropy. In such systems, the mixing time (the time for a phase space cell of size Planck's constant h to explore all of the available phase space on a mesh of that scale) scales only logarithmically with h, in contrast with the Heisenberg time, which scales as a power law. Thus, in the limit of small h a given classical system will always have a mixing time much shorter than the Heisenberg time, and many trajectories will exist linking any h-sized cell with any other well before individual eigenstates begin to be resolved. It is reasonable to conjecture [7] that for such systems individual eigen-

*kaplan@physics.harvard.edu

states will in fact evenly cover all of the available energy hypersurface, up to uncorrelated Gaussian fluctuations given by random matrix theory (RMT). Indeed, RMT does correctly predict much of the structure of eigenstates (and also the eigenvalue spectrum) of classically chaotic systems.

However, we also know that the Gutzwiller trace formula [8] is quite effective in using short periodic orbits to predict non-random fluctuations in the quantum spectra of classically chaotic systems. It is then not too surprising that the unstable periodic orbits of a chaotic system should also have a strong effect on the *eigenstate* structure, modifying RMT predictions. In fact, it appears that in the $\hbar \to 0$ limit, scarring constitutes the most important deviation from perfect ergodicity of chaotic eigenstates at the $\hbar$-scale, in the sense of RMT. Other deviations from RMT, such as dynamical localization, disappear in the semiclassical limit, but the scarring phenomenon survives. It, along with symmetry effects, is sufficient to explain quantitatively many properties of quantum chaotic systems, including wavefunction intensity statistics, wavefunction and phase space intensity correlations, channel-to-channel transport, resonance widths, and conductances.

We conclude this introduction by defining what we mean by scarring and addressing four common misconceptions about this phenomenon; our comments here may help to clarify issues which in the past have led to confusion and even controversy surrounding this subject.

(i) Scarring is defined as the anomalous enhancement or suppression of eigenstate intensity on or near an *unstable* periodic orbit and its invariant manifolds[1], in a chaotic system. Of course, stable periodic orbits also attract eigenstate intensity, as mentioned above, but the reasons for this are well understood in terms of the semiclassical theory of integrable systems [4]. More importantly, the increased tendency of a probability distribution launched in the vicinity of a stable orbit to overlap with itself at long times can be understood as a purely classical phenomenon. Phases are necessary only to obtain the quantization energies, in accordance with the WKB condition. On the other hand scarring can be thought of in the time domain as the increased probability of a quantum wavepacket launched near an *unstable* orbit to overlap with itself at very long times. Classical dynamics in a chaotic system shows no such behavior: classically an evolved probability distribution loses at long times all memory of its initial position. So scarring is at first sight a paradoxical phenomenon because its presence implies that quantum mechanics retains a much better memory at long times of short-time classical behavior than does long-time classical mechanics itself. This paradox, as we will see, is resolved by realizing that scarring is inherently an interference effect, and can only be understood by including phase information.

(ii) Scarring is a *statistically significant* deviation from single-channel quantum ergodicity, as defined by random matrix theory (which predicts uniform wavefunction amplitude over all of available phase space, up to Gaussian random fluctuations). Of course random enhancements in wavefunction intensity occur even in the absence of any periodic orbit; they can be observed, for example, in random superpositions of plane waves of constant energy [9]. Thus, anecdotal evidence, in the form of pictures of scarred states, is generally not a good way to test a theory of scarring, because even in RMT there is a finite probability to observe any given enhancement in one or a few states. An exception to this general rule arises when the instability exponent λ of a given periodic orbit is very small. Then as we shall see one expects to find many states (more precisely, a fraction of $O(\lambda)$ of all states) having enhancement factors of order $1/\lambda$ at this orbit, and each one of these individually has an exponentially small probability to occur within the context of RMT. For moderate λ, a few states will not produce the desired evidence of scarring, and one needs to consider the entire distribution of eigenstate intensities on the periodic orbit, sweeping through energy or some other parameter. This distribution can then be compared quantitatively with the scar theory prediction (which differs very significantly from RMT).

(iii) Scarring in not the same as the semiclassical evaluation of individual eigenstate intensities; rather it is a statistical property of states near a periodic orbit. It is true that in certain systems semiclassical methods work well all the way to the Heisenberg time, and can be used to resolve individual eigenstates [10]. However, this requires putting in at least as much information into the semiclassical calculation as there is in the full quantum system itself. Exact wavefunctions of individual states are sensitive to small changes in system parameters, and they provide no intuition about the overall behavior of the system. On the other hand, the statistical predictions of scar theory (concerning the distribution of wavefunction intensities, mean conductances and conductance fluctuations, mean resonance lifetimes, etc.) depend on only a few parameters (e.g., the exponent λ), and provide intuitively useful information about entire ensembles of chaotic systems which could not be obtained by using a computer to diagonalize a given Hamiltonian. The distinction is also very important experimentally because the scarring phenomenon is robust under small perturbations to the system; thus scar theory predictions will often be valid in situations where the exact dynamics is

[1]The invariant manifolds are the set of phase space points that classically approach the periodic orbit as $t \to +\infty$ (the *stable* manifold), and the set that approach the same orbit as $t \to -\infty$ (the *unstable* manifold). In a two-dimensional phase space, these are both curves, and the lines tangent to the curves at the periodic point are known as the stable and unstable directions, respectively. The (infinitely many) points of intersection of the stable and unstable manifolds are the *homoclinic* points of the orbit (see below).

not known well enough to allow individual eigenstates to be theoretically determined (either quantum mechanically or semiclassically).

(iv) Finally, as explained above, scars are not a threat to SZCdV ergodicity; scar theory addresses quantum structure at the $\hbar$-level and is to be properly compared with RMT, a much stronger condition than the quantum ergodicity of Schnirelman, Zelditch, and Colin de Verdiere.

The remainder of this paper is organized as follows: in the next section we briefly review some relevant experiments and discuss several theoretical approaches that have been used to understand scarring. Because the literature is extensive, it will not be possible to do full justice to the contributions of the various authors. The bulk of the present paper is a survey of results recently obtained using the wavepacket dynamics method, a project initiated by Heller in the seminal paper [2]. Of course, many or all of the results presented here can be understood also in the context of the other approaches, particularly in the context of Gutzwiller periodic orbit theory. However, as a unifying framework we choose to use the time-domain methodology in which the results were first obtained, and make contact with other points of view where appropriate.

Thus, Section III introduces and reviews the linear (short-time) and nonlinear (long-time) theory of scarring, as discussed in greater detail in [11]. The emphasis here is on developing the conceptual framework and describing the relations among the concepts of the Gaussian wavepacket, the short-time and long-time autocorrelation function, the local density of states (LDOS), the linearized energy envelope, and the inverse participation ratio (IPR). This machinery is put into use immediately in Section IV where we perform numerical tests and compare the data with quantitative theoretical predictions about spectra, IPR's, and energy correlations. An analysis of wavefunction intensity statistics [12] follows in Section V, where we find in accordance with scar theory a power-law tail in the intensity distribution, in sharp contrast with the exponential-tail prediction of RMT. Section VI addresses and resolves ambiguities in the measure of scarring intensity, leading to a universal and fully optimal measure in the strong scarring limit [13]. Section VII deals with more recent applications of scar theory to open systems, discussing resonances, the probability to remain in an open chaotic system [14], and the effect of scars on conductances [15]. Finally, in Section VIII we sum up the results and suggest some directions for the future.

II. EXPERIMENTAL EVIDENCE AND THEORETICAL PROGRESS

A. Experimental and numerical evidence for scars

Scarred eigenfunctions were first directly observed experimentally in two-dimensional microwave cavities by Sridhar [16], and independently by Stein and Stöckman [17]. Here one makes use of the exact correspondence between the quantum wavefunctions of a billiard system and the electromagnetic modes in a cavity with the same boundary conditions. The electromagnetic modes at various energies can be mapped either by measuring the reflected microwave power as a function of energy and position [17], or by using a perturbative technique involving measurements of small energy shifts [16]. Individual eigenstates scarred by specific short unstable orbits can be observed, although no attempt was made to quantify the scarring strengths. Of course, experimental limitations may preclude the collection of data at extremely high frequencies, where one could test scar theory predictions about the statistics of chaotic wavefunctions in the semiclassical limit.

Another very important set of experiments [18] have been performed in semiconductor heterostructures. A resonant tunneling device contains a quantum well separated by a barrier from a two-dimensional electron gas. Electrons can be injected into the quantum well, and information about electron wavefunctions obtained by studying the tunneling rates. When a large tilted magnetic field is turned on, the classical dynamics of the system is known to be chaotic. Indeed, very strongly scarred wavefunctions are observed in such systems, associated with orbits that have a small instability exponent for a wide range of system parameters [19]. Again, the scarring patterns are in good qualitative agreement with theoretical expectations.

Given the difficulty in collecting large amounts of good experimental data at very high energies, numerical simulations of quantum chaotic systems have from the very beginning been useful in providing "empirical" support for the scarring phenomenon. Many different quantum chaotic systems have been thus explored, including, for example, the hydrogen atom in a uniform magnetic field [20]. In recent work by Li and Hu [21], a plane wave decomposition method is used to find wavefunctions near the one-millionth state of the stadium billiard, showing that strong scarring is still present at such energies. Certain orbits, including the diamond orbit, are observed to be scarred in a corridor of width scaling as the wavelength (rather than as the geometric mean of the wavelength and the system size; see below). The reason for this is not well understood by the present author, though it may be associated with the very special properties of the stadium, namely, the presence of marginally stable orbits and intermittency.

A statistical analysis of intensities in highly-excited wavefunctions of the stadium and other hard chaotic systems would prove very useful; such a detailed analysis of medium-energy wavefunctions in phase-space co-

ordinates on the billiard boundary is now in preparation [22]. A somewhat different point of view is taken by Bäcker, Schubert, and Stifter [23], who examine the approach to SZCdV quantum ergodicity in position space for various chaotic billiards (again, in a medium energy range). Simonotti, Vergini, and Saraceno [24] have studied scar intensity on the boundary of a stadium billiard, using a phase-space representation and also considering improved test states which are superpositions of *several* phase-space Gaussians (see Section VI).

B. Several theoretical approaches

The first theoretical explanation of the scarring phenomenon is found already in [2], where a Husimi space measure of scar strength is used. In this approach (which we discuss at much greater length beginning with the following section), wavefunction intensity in phase space is defined by the squared overlaps of the wavefunction with Gaussian wavepackets $|a^{q_0,p_0}\rangle$ centered at all possible phase space points (q_0, p_0). If we consider one such Gaussian and look at its squared overlaps with all eigenstates of the system, we obtain a local density of states at the location of that wavepacket

$$S^{q_0,p_0}(E) = \sum_n |\langle n|a^{q_0,p_0}\rangle|^2 \, \delta(E - E_n) \, . \tag{1}$$

What Heller realized was that the autocorrelation function of the wavepacket,

$$A^{q_0,p_0}(t) = \langle a^{q_0,p_0}|a^{q_0,p_0}(t)\rangle \, , \tag{2}$$

the Fourier transform of the spectrum $S(E)$, shows large recurrences at short times which are integer multiples of the orbit period T_P, if the point (q_0, p_0) is on or near a periodic orbit of the system. The strength of these recurrences falls off exponentially with time, roughly as $e^{-\lambda t/T_P}$, where λ is the instability exponent of the unstable periodic orbit. In the semiclassical limit $\hbar \to 0$, these periodic recurrences (both amplitudes and phases) can be easily analytically computed in terms of the classical stability matrix and the classical action of the periodic orbit. The recurrences are called "linear", as they are obtained by linearizing the dynamics around the unstable periodic orbit in question. This short-time structure in $A(t)$ produces an envelope in the spectrum $S(E)$ which must be the smoothed version of the true LDOS at the periodic orbit. Thus, by considering only the short-time dynamics of the Gaussian wavepacket, we obtain an energy-smoothed LDOS,

$$S^{q_0,p_0}_{\rm smooth}(E) = \sum_n |\langle n|a^{q_0,p_0}\rangle|^2 w(E - E_n) \tag{3}$$

from which we can easily extract the average wavefunction intensity near various energies. If the exponent λ is small, the smoothed LDOS is shown to have a sequence of bumps separated by $2\pi\hbar/T_P$ and of width scaling as $\lambda\hbar/T_P$. At these optimal scarring energies (which are analogous to the EBK energies for an integrable system), wavefunctions must, on average, have larger than normal intensities on the periodic orbit, while far from these spectral peaks wavefunctions must be typically antiscarred, i.e. have less than expected intensity on the same orbit.

The linear theory of scarring provides information only about the average wavefunction intensity in some energy range; it does not tell us whether most of that intensity is contained in a few wavefunctions (the "totalitarian" scenario) or whether it is equally distributed among all the wavefunctions near that energy (the "egalitarian" scenario). For this, we need a nonlinear theory of scarring, one that takes into account long-time recurrences in the autocorrelation function $A(t)$. These recurrences correspond to pieces of the wavepacket leaving the vicinity of the periodic orbit, traveling through other regions of phase space where they are subjected to complicated chaotic dynamics, and eventually returning to the periodic orbit. In many situations, these long-time recurrences may be treated statistically, producing a separation of scales between the classically-obtained short-time behavior near the periodic orbit and the random long-time behavior, as suggested already by Antonsen et al. [25]. What is important to note here is that the short-time behavior must necessarily leave an imprint on the long-time behavior and on stationary properties like the LDOS, as we will see more clearly in the following section.

First, we briefly mention some alternative theoretical approaches to the scarring problem, which provide useful and complementary perspectives on the subject. A theory of wavefunction scarring in position space has been developed by Bogomolny [26]; clearly the position space basis is a very relevant one for many experimental applications. Bogomolny again smoothes the wavefunction intensity over some small energy range ΔE,

$$< |\psi(q)|^2 >_{\Delta E} = \frac{1}{N} \sum_n |\psi_n(q)|^2 \, , \tag{4}$$

and (in the semiclassical limit $\hbar \to 0$) represents this smoothed intensity as a sum over periodic trajectories of the system:

$$< |\psi(q)|^2 >_{\Delta E} = \rho_0(q) + \hbar^{(n-1)/2} \times \sum_p {\rm Im} \left\langle B_p(z) \exp\left(i\frac{S_p}{\hbar} + i\frac{W_p^{km}(z)}{2\hbar} y_k y_m \right) \right\rangle_{\Delta E} \, . \tag{5}$$

For each periodic orbit p, z is chosen to be a coordinate along the orbit, while the y_m $(m = 2 \ldots n)$ are all the coordinates perpendicular to the orbit. S_p is the classical action around the orbit, while B_p is a focusing factor which can be easily obtained from the stability matrix of the orbit (i.e. from the linearized dynamics

for small $y, \dot{y}$). Similarly W_p^{km} measures the quadratic change in the action for small values of y, as one moves away from the orbit. It is important to note here that the sum in Eq. 5 is effectively finite: any orbits of period $T_p >> \hbar/\Delta E$ can be dropped as their oscillatory contribution vanishes when integrated over the smoothing interval ΔE. As ΔE becomes small, more and more orbits need to be included in the sum (the number of orbits grows exponentially with period T_p in a chaotic system). The constant $\rho_0(q)$ term can be thought of as coming from the zero-time dynamics of the system; it is related to the mean density of states at energy E. Bogomolny computes the oscillatory contributions to the above sum from various short periodic orbits in the stadium billiard and finds qualitative agreement with numerical data.

Bogomolny's semiclassical Green's function approach is clearly closely related to our wavepacket dynamics method, as the semiclassical Green's function can be obtained from the semiclassical time-domain propagator by a stationary-phase Fourier transform. One difference between the approaches is that Bogomolny envisions summing over a large number of periodic orbits to get as close as possible to an energy domain resolution of order of a mean level spacing. As mentioned above, in some systems it is indeed possible to use semiclassical methods to compute individual eigenstates of the system [10]. In fact for this purpose one needs information only about orbits of period up to the mixing time (which scales logarithmically with $\hbar$) rather than the Heisenberg time (which scales as a power law). However, our aim here is to make predictions about the distribution of scarring strengths based only on linearized information around *one* periodic orbit; for this purpose most other orbits which produce additional oscillations in the density of states may be treated statistically [25]. It is important to note in this context that if we are measuring wavefunction intensities on a given orbit p of period T_p, then in the semiclassical limit there are no short orbits that come close to this orbit (on a scale of $\hbar$) in phase space. The only oscillatory contributions which will need to be taken into account are from orbits closely related to orbits *homoclinic* to p [homoclinic orbits are those that approach p at large negative times, perform an excursion away from p into other regions of phase space, and then again approach p at large positive times]. In fact, in the $\hbar \to 0$ limit the periodic orbit sum (Eq. 5) for a point q on a given periodic orbit p can be written equivalently as a contribution from orbit p itself plus a sum over trajectories homoclinic to p. Although the two points of view are mathematically equivalent, the homoclinic sum approach makes explicit the special role of the orbit p near which we are making measurements.

We also take this opportunity to note that a position space basis, though obviously physically natural in many measurement situations, is not generally an optimal one for detecting scar effects. Unless the periodic point q happens also to be a focusing point of classical trajectories near the orbit, only a small fraction of the total scar strength is captured in the position basis, and the fraction becomes smaller as $\hbar$ decreases (or as the energy increases). An easy way to see this is to notice that the effects of a classical trajectory in quantum mechanics *generically* extend to a region around the orbit scaling not as a wavelength but rather as the square root of a wavelength (and similarly the affected region scales as the square root of the total number of channels in momentum space). Thus, unless either the stable or unstable manifold of the orbit p at periodic point q happens to be oriented along the momentum direction, the position space basis will not be optimal, as reflected in the falling off of the focusing prefactor B_p with energy (and similarly the momentum basis will not be optimal, unless one of the two invariant manifolds is oriented along the position direction). All this will become more clear in the exposition of the following section. In any case, one should keep in mind that a position space basis can always be considered as a special limiting case of the Gaussian wavepacket test state, where the position uncertainty of the wavepacket becomes comparable to a wavelength, and the momentum uncertainty becomes large.

Wigner phase space analysis of the scarring phenomenon was pioneered by Berry [27]. Berry considers the Wigner spectral function, $W(x, E, \Delta E)$, again smoothed over an energy interval ΔE near E. $x = (q_0, p_0)$ is a phase space point. Being formulated in phase space, the approach more closely resembles that of Heller, and working in Wigner phase space instead of Husimi space also eliminates the need to choose the (apparently arbitrary) eccentricity and orientation of the Gaussian wavepackets a^{q_0,p_0}. The downside of Wigner phase space is the absence of a positivity condition on W; thus the value of the spectral function cannot be considered as corresponding to an intensity or a probability of being found near a certain point x (and random matrix theory is therefore not applicable). The Husimi function, which is manifestly positive definite, can be thought of as a phase space smoothing of the Wigner distribution over a phase space region scaling as $\hbar$. The ambiguity in choosing the Gaussian centered on x over which this smoothing is to be performed is indeed an important issue, to be considered carefully towards the end of the following section. There we will see that to obtain the *maximal* scarring effect, the Gaussian must be chosen to be properly oriented along the stable and unstable directions at the periodic point. [An arbitrarily large wavepacket width is allowed along either of these directions, with a correspondingly small width in the orthogonal direction. Also, strong, but non-maximal, scarring will generally be obtained for any wavepacket with width scaling as $\sqrt{\hbar}$ in both the position and momentum directions.] See also Section VI for a discussion of even better measures of scarring possible if one is willing to go beyond the Gaussian wavepacket approximation.

Berry studies carefully the structure of the spectral Wigner function W as x moves off the closed orbit within the energy hypersurface and also as x moves off the en-

ergy surface itself (the fringes he obtains disappear upon Husimi averaging). In particular, as x moves off the periodic orbit, the transverse oscillations take the form of a complex Gaussian, with fringe spacing scaling as $\sqrt{\hbar}$. The amplitude of the fringes depends only on the stability matrix, although the precise pattern changes as one moves along the orbit. In a two-dimensional phase space, the fringes form hyperbolas approaching the stable and unstable manifolds of the orbit.

A common limitation of the analyses [2,26,27] is that they make no predictions about the properties of the spectral fluctuations on scales much smaller than $\hbar/T_D$, where $T_D \sim T_P/\lambda$ is the decay time of the unstable orbit being studied. Therefore is it not possible to make quantitative predictions about individual wavefunction intensities, participation ratios, etc., without explicitly doing a Gutzwiller sum over *all* periodic orbits. Even if the sum can be performed, it is by no means clear that it will converge in all cases (e.g. in systems where caustics are important [28]). When the sum does converge it may produce individual semiclassical wavefunctions very different from the quantum eigenstates, due to diffraction and other "hard quantum" effects. Furthermore, as we discussed in the introduction, such Heisenberg-time calculations are extremely sensitive to small perturbations on the system. What one would like is to be able to say precisely how often a given single-wavefunction scar strength will appear on a given orbit, at what energy, and at what parameter values. In the semiclassical limit, this can in fact be done using only information about linearized dynamics near the orbit itself, and, in some cases, about a few strong isolated homoclinic recurrences which cannot be treated statistically.

Before proceeding to the main part of the paper, we mention some of the important contributions to scar theory since the early work of Heller, Bogomolny, and Berry. Many different aspects of the scarring phenomenon have been theoretically investigated, and we here mention only a few which are most relevant to the present work. Agam and Fishman [29] define the weight of a scar by integrating the Wigner function over a narrow tube in phase space, of cross-section $\hbar$, surrounding the periodic orbit. The Fredholm method can be used to obtain a semiclassical formula for scars. Alternatively, de Polavieja, Borondo, and Benito [30] construct a test state highly localized on a given periodic orbit using short-time quantum dynamics. We defer all discussion of improved measures of scarring beyond the simple Gaussian wavepacket measure until Section VI, where this important issue is treated in full generality.

Klakow and Smilansky [31] have used a scattering approach to quantization to study the wavefunctions of billiard systems. They treat carefully the wavefunctions on the Poincare surface of section, and relate their properties to scarring in configuration space. de Almeida [32] uses the Weyl representation to establish connections between classical and quantum dynamics, with particular application to the semiclassical Wigner function and scars. Tomsovic [33] has used parametric variation as a new method for studying scar effects; scars are shown to induce correlations between wavefunction intensities on a periodic orbit and the level velocities of these wavefunctions when certain system parameters are varied. We also mention the work of Arranz, Borondo, and Benito [34] who have probed the intermediate region between regular and strongly chaotic quantum behavior, and have shown how scarred states first arise from the mixing of pairs of regular wavefunctions as $\hbar$ is decreased (but well before one reaches the semiclassical limit which is the main focus of the present review). Finally, several groups [35–37] have studied the hyperbolic scar structures associated not only with the periodic orbit itself but with its invariant manifolds and homoclinic orbits. This subject we also return to in Section VI.

III. LINEAR AND NONLINEAR THEORY OF SCARRING

Consider an arbitrary (unstable) periodic orbit of a chaotic system. We will simplify the initial exposition by taking the orbit to be a fixed point of a discrete-time area-preserving map on a two-dimensional phase space. [The case of a higher-period orbit of such a map, or of an orbit of a continuous-time dynamics in two spatial dimensions, can be reduced to the present case simply by iterating the original map, or by taking a surface of section map, respectively. The generalization to these two situations is straightforward, and is discussed towards the end of this section and in more detail in [11]. Similarly, the entire framework generalizes with minor modifications to unstable orbits in higher-dimensional systems.]

The fixed point is taken to be at the origin of phase space, $(q,p) = (0,0)$. Without loss of generality, we can take the stable and unstable directions at the fixed point to be vertical (p) and horizontal (q), respectively. The local dynamics around the periodic orbit can always be put into this form via a canonical transformation of the coordinates. Then the only parameter describing the local (linearized) dynamics near the orbit is λ, the instability exponent for one iteration of the orbit. Locally, the equations of motion are given by

$$\begin{aligned} q &\to \tilde{q} = e^{\lambda t} q \\ p &\to \tilde{p} = e^{-\lambda t} p \,. \end{aligned} \tag{6}$$

We are interested in studying the behavior of the quantum wavefunctions near this fixed point; as discussed earlier the natural way to do this is by examining their overlaps with a phase-space Gaussian centered on this point:

$$a_\sigma(q) = \left(\frac{1}{\pi\sigma^2\hbar}\right)^{1/4} e^{-q^2/2\sigma^2\hbar} \,. \tag{7}$$

This is a minimum-uncertainty state centered at the origin of phase space, with width $\sigma\sqrt{\hbar}$ in the $q-$direction

and $\sqrt{\hbar}/\sigma$ in the $p-$direction. The width σ is an arbitrary parameter: σ^2 is the aspect ratio of the phase-space Gaussian, typically chosen to be of order unity. Any real value of σ, as we shall soon see, produces a wavepacket capable of optimally measuring scar strength. The apparent ambiguity in the choice of σ is an important issue that we will return to in Section VI.

In fact, there is another, less obvious, ambiguity in the choice of the test wavepacket in Eq. 7. A non-circular Gaussian can be made to have any desired orientation in the $q-p$ plane by complexifying σ; this produces a test state in which q and p are correlated. Any Gaussian which is not oriented along the stable and unstable axes (p and q, in our example) will be non-optimal in the sense of having smaller short-time recurrences in its autocorrelation function $A(t)$ compared with an optimal wavepacket, and therefore having also smaller fluctuations in its spectral intensities $|\langle n|a\rangle|^2$. A wavepacket defined to be circular in a coordinate system in which the two invariant directions are *not* orthogonal will be transformed into such a "tilted" wavepacket in our preferred coordinate system (Eq. 6) defined by the stable and unstable directions. Also, a position or momentum state will generically appear "tilted" in this preferred coordinate system of the periodic orbit. See Eq. 25 below, and the associated discussion.

For small enough $\hbar$, the wavepacket $|a_\sigma\rangle$ and its short-time iterates are contained well within the linear regime. As long as the wavepacket stays in the phase space region surrounding the periodic orbit in which the linearized equations of motion (Eq. 6) apply, the evolution of the wavepacket is completely semiclassical, given simply by the stretching of the $q-$width parameter σ (and the associated shrinking of the momentum-width $\sigma_p = \sigma^{-1}$). More explicitly, at short times we have

$$U^t|a_\sigma\rangle \approx U^t_{\rm lin}|a_\sigma\rangle = e^{-i\phi t}|a_{\sigma e^{\lambda t}}\rangle\,, \tag{8}$$

where U is the unitary operator implementing the quantum discrete-time dynamics, $U_{\rm lin}$ represents the quantization of the linearized behavior near the periodic orbit, and t is time, measured in units of a single mapping. Here $-\phi$ is a phase associated with one iteration of the periodic orbit: it is given by the classical action in units of $\hbar$, plus Maslov indices if appropriate.

Then the short-time autocorrelation function of the wavepacket is easily seen from Eqs. 7,8 to have the form

$$A_{\rm lin}(t) = e^{-i\phi t}\langle a_\sigma|a_{\sigma e^{\lambda t}}\rangle = \frac{e^{-i\phi t}}{\sqrt{\cosh(\lambda t)}}\,. \tag{9}$$

The 'lin' subscript indicates that Eq. 9 describes the piece of the autocorrelation function coming from the linearized dynamics around the periodic orbit. For a weakly unstable orbit (small λ), $A_{\rm lin}(t)$ is slowly decaying, with strong recurrences happening for the first $O(1/\lambda)$ iterations of the orbit. We note that the short-time autocorrelation function $A_{\rm lin}(t)$ is σ-independent (for real σ), a fact that will prove important later on.

After a certain time, the wavepacket leaves the linearizable region and nonlinear recurrences begin to dominate the return probability. This time scale, called the log-time, scales logarithmically in $N \sim \hbar^{-1}$ because of the exponential divergence of trajectories away from the orbit:

$$T_{\log} \sim \frac{\log fN}{\lambda}\,. \tag{10}$$

Here N is the total number of h-sized cells in the accessible phase space (also equal to the dimension of the effective quantum mechanical Hilbert space), and f is the fraction of this phase space (typically $O(1)$) in which the linearized equations of motion (Eq. 6) apply. Semiclassically, the long-time recurrences are given by a sum over all trajectories homoclinic to the original periodic orbit. These are classical trajectories that as $t \to -\infty$ approach the fixed point along the unstable manifold (the q-axis, in our case), and as $t \to +\infty$ approach it again, this time along the stable manifold (p). Let us choose a point $x = (\delta q, 0)$ on the unstable axis which is well within the linearizable region surrounding $(0,0)$, and which after T time steps maps to a point $f^T(x) = (0, \delta p)$ on the stable axis, again inside the linearizable regime. In between the trajectory must undergo some complicated nonlinear behavior in phase-space regions far from the fixed point.

The path of the full trajectory and its surroundings naturally separates into three stages: (i) τ_1 steps during which a thin vertical strip centered on x of the original wavepacket shrinks vertically and stretches horizontally as its center moves out horizontally at an exponential rate along the unstable manifold, finally reaching the edge[2] of the linearizable region; followed (ii) by complicated nonlinear dynamics for $T-\tau_1-\tau_3$ steps, which eventually brings the center of the distribution back into the linearizable region; and finally (iii) a time of τ_3 steps during which the dynamics takes us back through the linearizable region, this time along the stable direction. After T steps, the original thin vertical strip has become a long horizontal strip which then intersects the original Gaussian. The total contribution to the wavepacket autocorrelation function at time T coming from this homoclinic excursion is given by a product of five factors:

$$\begin{aligned} A_{\mathcal{HC}} = {} & e^{-\delta q^2/2\sigma^2}\cdot e^{-i\tau_1\phi}e^{-\lambda\tau_1/2} \\ & \cdot\ Q(T-\tau_1-\tau_3)e^{i\phi_{\rm nonlin}} \\ & \cdot\ e^{-i\tau_3\phi}e^{-\lambda\tau_3/2}\cdot e^{-\delta p^2/2\sigma_p^2}\,. \end{aligned} \tag{11}$$

The factors $e^{-\lambda\tau_1/2}$ and $e^{-\lambda\tau_3/2}$ are instability factors associated with the linearized motion of the wavepacket,

[2] Of course, the exact boundaries of the linearizable region are arbitrary and in no way affect the final result. All that is required is for the wavepacket itself to be well-contained in the region where the linearized equations of motion hold.

while $e^{-i\tau_1\phi}$ and $e^{-i\tau_3\phi}$ are the corresponding phases. The suppression factors $e^{-\delta q^2/2\hbar\sigma^2}$ and $e^{-\delta p^2/2\hbar\sigma_p^2}$ result from the fact that the initial and final points of the excursion are both off-center relative to the Gaussian wavepacket (recall $\sigma_p = 1/\sigma$). The total correlation function $A(T)$ is given semiclassically by a sum of terms of the form (Eq. 11) over all the homoclinic excursions of length T:

$$A_{\rm SC}(T) = \sum_{\mathcal{HC}} A_{\mathcal{HC}}\,. \tag{12}$$

Because the long-time homoclinic orbits come back with complicated accumulated phases $\phi_{\rm nonlin}$, and the number of these recurrences grows exponentially with time, one might expect the total long-time return amplitudes to be given by Gaussian random numbers. In fact, however, we must consider together contributions from all homoclinic excursions which lie on a single homoclinic orbit, e.g. the trajectory which takes $x \to f^T(x)$ in T steps and the one which takes $f^{\Delta_1}(x) \to f^{T+\Delta_2}(x)$ in $T + \Delta_2 - \Delta_1$ steps, where Δ_1 and Δ_2 are small enough that the resulting phase-space points are still in the linearizable regime. These paths all come back in phase with each other, having the same nonlinear phase $\phi_{\rm nonlin}$, and give rise to short-time correlations in $A(t)$ for large t [11]. These correlations are shown to be related to the short-time dynamics of the original Gaussian wavepacket. In fact, we can write the return amplitude at times $T_{\log} \ll T \ll T_H$ ($T_H = N$ is the Heisenberg time, where individual eigenstates begin to be resolved) as a convolution

$$A(T) = \sum_{\tau} A_{\rm rnd}(\tau) A_{\rm lin}(T-\tau)\,. \tag{13}$$

Here $A_{\rm lin}$ is the short-time return amplitude, and $A_{\rm rnd}$ has the statistical properties of an uncorrelated random Gaussian variable. In particular,

$$\begin{aligned} < A_{\rm rnd}(\tau) > \; &= 0 \\ < A^\star_{\rm rnd}(\tau) A_{\rm rnd}(\tau') > \; &= \frac{1}{N}\delta_{\tau\tau'}\,. \end{aligned} \tag{14}$$

The prefactor $1/N$ provides the proper classical normalization: in the absence of interference effects, the probability to come back is equal to the probability for visiting any other state in the Hilbert space. The average in Eq. 14 is taken over long times τ, $T_{\log} \ll \tau \ll T_H$, and/or over an ensemble of systems which all have the same linearized dynamics around our chosen periodic orbit. In either case, the total size of the Hilbert space N ($= 1/h$ for a phase space area normalized to unity) has been assumed to be large. We then obtain

$$\begin{aligned} < A(t) > \; &= 0 \\ < A^\star(t) A(t+\Delta) > \; &= \frac{1}{N}\sum_s A^\star_{\rm lin}(s) A_{\rm lin}(s+\Delta)\,. \end{aligned} \tag{15}$$

At times beyond the Heisenberg time, this gets modified [11] to

$$< A^\star(t) A(t+\Delta) >= \frac{F}{N}\sum_s A^\star_{\rm lin}(s) A_{\rm lin}(s+\Delta)\,. \tag{16}$$

F is a factor associated with the discreteness of the eigenstates: it is 3 for real eigenstate–test state overlaps and 2 for complex overlaps.

The long-time autocorrelation function is thus self-correlated on a scale $\Delta \sim \lambda^{-1}$. Qualitatively, this can be understood on a purely classical level: once probability happens to come back to the vicinity of a weakly unstable periodic orbit, it tends to stay around before leaving again. On the other hand, the overall enhancement in the total return probability at long times:

$$< |A(t)|^2 >= \frac{F}{N}\sum_s \frac{1}{\cosh(\lambda s)}\,, \tag{17}$$

obtained by combining the general expression Eq. 16 with the short-time overlap dynamics of the Gaussian wavepacket (Eq. 9), is fundamentally an interference phenomenon, and signals a kind of quantum localization. In terms of homoclinic orbits, the enhancement arises because of the coherent addition of paths of the same length T lying on the same homoclinic orbit (setting $\Delta_1 = \Delta_2$ in the discussion following Eq. 12).

We now define $S(E)$ to be the Fourier transform of the autocorrelation function,

$$S(E) = \frac{1}{2\pi}\sum_{t=-\infty}^{+\infty} A(t) e^{iEt}\,. \tag{18}$$

For a non-degenerate spectrum, it is easy to see (by inserting a complete set of eigenstates) that this produces the line spectrum of Eq. 1. Cutting off the sum in Eq. 18 at $\pm T_{\log}$, or equivalently by including only linearized dynamics around the periodic orbit, we obtain *the smoothed local density of states*:

$$S_{\rm lin}(E) = \sum_t A_{\rm lin}(t) e^{iEt}\,, \tag{19}$$

an envelope centered at quasienergy $E = \phi$ (see Eq. 9), of width $\delta E \sim \lambda$, and of height $\sim \lambda^{-1}$ (a factor of 2π has been inserted into the definition of $S_{\rm lin}$ for future convenience). $E = \phi$ is the analogue of the EBK quantization condition for integrable systems; here, because of the instability of the orbit, scarred states can live in an energy range of $O(\lambda)$ around the optimal energy. States with energy more than $O(\lambda|\log\lambda|)$ away from resonance tend to be *antiscarred*, i.e. they have less than expected intensity at the periodic orbit [see Eq. 67 and Fig. 11].

Now long-time (nonlinear) recurrences as in Eq. 13 lead to fluctuations under the short-time envelope in the full spectrum $S(E)$. Because these recurrences involve a random variable *convoluted* with the short time dynamics, in the energy domain we obtain random fluctuations

multiplying the short-time envelope. (It is easy to see physically that the random oscillations must multiply the smooth envelope: if they were merely added to it, the total spectrum would go negative away from the peak of the envelope.) Finally, at the Heisenberg time $T_H = N$, individual states are resolved [11,12], and we see a line spectrum (Eq. 1) with a height distribution given by

$$I_{na_\sigma} \equiv |\langle n|a_\sigma\rangle|^2 = r_{an} S_{\rm lin}(E_n)\,. \tag{20}$$

Here r_{an} are random variables (with mean $< r_{an} >= 1/N$) drawn from a chi-squared distribution of one degree of freedom (two degrees of freedom for complex $\langle n|a_\sigma\rangle$). Thus we obtain a random (Porter-Thomas) line spectrum, multiplying the original linear envelope [see Fig. 1 for a numerical example].

We now need to discuss the concept of an inverse participation ratio (IPR), a very useful measure for studying deviations from quantum ergodicity. We define

$$\mathrm{IPR}_{a_\sigma} = N \sum_n I_{na_\sigma}^2 = N \sum_n |\langle n|a_\sigma\rangle|^4\,. \tag{21}$$

(Note that $\sum_n I_{na_\sigma} = 1$ by normalization.) Being the first non-trivial moment of the eigenstate intensity (I_{na_σ}) distribution, the IPR provides a convenient one-number measure of the strength of scarring (or any other kind of deviation from quantum ergodicity). The IPR would be unity for a wavepacket that had equal overlaps with all the eigenstates of the system; the maximum value of N is reached in the opposite (completely localized regime), when the wavepacket is itself a single eigenstate. Random matrix theory predicts an IPR of F, the strong quantum ergodicity factor defined above in Eq. 16.

However, from Eqs. 1,18 we see that

$$\mathrm{IPR}_{a_\sigma} = \lim_{T\to\infty} \frac{N}{T} \sum_{t=0}^{T-1} |A(t)|^2\,; \tag{22}$$

as one might expect, localization is associated with an enhanced return probability at long times. Now from Eq. 17 we see that scar theory predicts an enhancement in the IPR over random matrix theory:

$$\mathrm{IPR}_{a_\sigma} = F \sum_s \frac{1}{\cosh(\lambda s)} \to F\frac{\pi}{\lambda}\,, \tag{23}$$

where the limit of small λ has been taken. (F, as before, is 3 or 2, depending on whether the states are real or complex, respectively.) The IPR thus decomposes into a product of two contributions: the shape of the short-time envelope coming from linear dynamics around the periodic orbit, and a quantum fluctuation factor F, as predicted by Porter-Thomas statistics. See Fig. 2 in the following section for numerical evidence in support of this prediction.

Before concluding this section, we briefly mention several straightforward generalizations of the above analysis. Eq. 9 for the short-time autocorrelation function $A_{\rm lin}$ and the linear spectral envelope $S_{\rm lin}$ which follows from it apply to a fixed point of a discrete-time map, but the analysis extends easily to higher-period orbits and to dynamics in continuous time. For a period T_P orbit of a map, the linearized autocorrelation function of an optimally oriented wavepacket takes the form

$$A_{\rm lin}(t) = \frac{e^{-i\phi t/T_P}}{\sqrt{\cosh(\lambda t/T_P)}} \delta_{t \bmod \mathrm{T_P},0}\,, \tag{24}$$

where λ is now of course the instability exponent for one iteration of the *entire* orbit, and ϕ the corresponding phase. This result is the same on each of the periodic points of the orbit; however, the optimal Gaussian wavepacket will in general have a different orientation at each point, due to the rotation of the invariant manifolds as one moves along the orbit. The resulting smoothed local density of states $S_{\rm lin}$ then has T_P peaks in the quasienergy interval $[0, 2\pi)$, each with a height scaling as λ^{-1} as before (in the regime of small instability $\lambda \ll 1$), and a width scaling as λ/T_P. Notice that the time and quasienergy coordinates have been simply rescaled by T_P; the ratio of scar peak separation to peak width, as well as the inverse participation ratio, remain independent of the period T_P, both scaling simply as λ^{-1}.

For a continuous-time Hamiltonian dynamics, the spectral envelope has infinitely many peaks, with energy spacing $\hbar/T_P$, height scaling as λ^{-1} as before, and width scaling as $\hbar\lambda/T_P$ for small λ. The positions of the peaks correspond of course to the EBK quantization condition along a stable orbit, and the widths can be thought of as resonance widths due to the instability of the orbit. In the semiclassical limit, more and more states are found under each of the scarring peaks, and the individual line heights are distributed in accordance with Eq. 20 (see [22] for a numerical example in the stadium billiard). The continuous-time dynamics also contains an additional time scale not found in the discrete-time system, namely the time $T_{\rm free}$ for the test wavepacket to traverse itself near $t = 0$ and again every time it returns to the vicinity of its original location. Thus, the δ-function sum in Eq. 24 must, for a continuous-time dynamics, be convoluted with a very short-time window of width $T_{\rm free}$ ($T_{\rm free} \ll T_P$ in the semiclassical limit). In the energy domain, this results in the infinite sequence of scarring peaks being multiplied by a very broad envelope of width $E_{\rm free} = \hbar/T_{\rm free}$. $E_{\rm free}$ is the energy uncertainty of the test wavepacket a_σ ($E_{\rm free} \sim p\sqrt{\hbar}\sigma_p = p\sqrt{\hbar}/\sigma_z$), and evidently depends on σ_z, the position-uncertainty of the wavepacket in units of $\sqrt{\hbar}$ along the direction of the orbit. This broad energy envelope is a classical effect (i.e. a classical phase-space distribution corresponding to the quantum wavepacket has this distribution of energies), and must first be taken into account before deviations from quantum ergodicity, such as scarring, can be analyzed. See [11,13,38] for a more complete discussion of these issues.

The individual peak height distribution (Eq. 20) in the

local density of states applies in the semiclassical limit for a hard chaotic system. In this limit, the homoclinic (nonlinear) recurrences are all weak, and no individual recurrence can affect significantly either a particular eigenstate or statistical wavefunction properties such as the IPR. However, at finite $\hbar$ it is quite possible for a certain class of identifiable homoclinic recurrences at medium times $T_{\rm med}$ to have a significant effect on the spectrum. The contributions from these special recurrences can then be computed analytically, and an improved spectral envelope created which takes into account not only the periodic orbit dynamics on scale T_P/λ, but also the special strong recurrences at the time scale $T_{\rm med}$. The general procedure, discussed in more detail in [11], is a sequential analysis of the various time scales, beginning with the shortest times. Thus, we start with the classical envelope coming from the free dynamics on time scale $T_{\rm free}$, then we include the effects of the short periodic orbit on which our wavepacket is located, then the effect of any special class of strong homoclinic recurrences (an $\hbar$-dependent contribution), and finally the effects of random recurrences at long times, all the way to the Heisenberg time T_H. In [11] an example is given of a system where the phase-space mixing away from the periodic orbit being studied is slow, so that at finite $\hbar$ very distinct oscillations in the LDOS at the orbit are obtained which can be assigned to a special class of intermediate-time recurrences.

The expression (Eq. 9) is valid, as we have discussed, for any wavepacket optimally oriented along the invariant manifolds of the periodic orbit. There is a one-parameter family of such optimal wavepackets at each periodic point: in the coordinate system of Eq. 6 in which the stable and unstable directions are orthogonal, this free parameter is the width of the Gaussian along either of the two directions. Gaussians that are tilted relative the invariant directions are non-optimal: the degree of non-optimality can be described by a single parameter $Q \geq 0$. This is easy to see by transforming to a coordinate system in which the chosen Gaussian is circular: in this coordinate system, Q is a function of the angle between the stable and unstable directions ($Q = 0$ for a right angle and increases as the angle decreases to 0). In the coordinate system in which the manifolds are orthogonal, Q will be a function of the aspect ratio of the Gaussian and its tilt relative to the axes. The general form of the short-time autocorrelation function is then

$$A_{\rm lin}(t) = \langle a|a(t)\rangle = \frac{e^{-i\phi t}}{\sqrt{\cosh\lambda t + iQ\sinh\lambda t}}\,. \qquad (25)$$

As long as Q is not large, the qualitative scarring behavior is unchanged, although spectral oscillations become less pronounced and there is less scarring and antiscarring as Q increases. Analytic results are less easy to obtain for non-zero Q, but quantitative predictions can be readily produced for comparison with any experimental or numerical data. See [14] for a discussion of the effect that non-zero Q has on antiscar strength, and thus on the probability to remain in a weakly open system.

Finally, we conclude this section by mentioning that the analysis can be easily extended to test-states centered off of the periodic orbit. In the coordinate system defined by Eq. 6, we may take a Gaussian centered at (q_0, p_0), with width $\sigma\sqrt{\hbar}$ in position space and $\sigma_p\sqrt{\hbar}$ in momentum (where $\sigma_p = 1/\sigma$):

$$a_\sigma(q) = \left(\frac{1}{\pi\sigma^2\hbar}\right)^{1/4} e^{-(q-q_0)^2/2\sigma^2\hbar + ip_0(q-q_0)}\,. \qquad (26)$$

Then the autocorrelation function is given by [39]

$$A_{\rm lin}(t) = \frac{\exp\left[-\frac{\sinh^2\lambda t/2}{\cosh\lambda t}(q_0^2/\sigma^2\hbar + p_0^2/\sigma_p^2\hbar)\right]}{\sqrt{\cosh\lambda t}} \times e^{-i\phi t - i(\tanh\lambda t)q_0p_0/\hbar}\,. \qquad (27)$$

We easily see that the linear recurrences, and thus scarring, are strong in a region of size $\sigma\sqrt{\hbar}\times\sigma_p\sqrt{\hbar} = \hbar$ in phase space. Eq. 27 will be made use of in Section V, where the tail of the wavefunction intensity distribution is obtained, summing contributions from test states located everywhere in phase space.

IV. QUANTITATIVE TESTS

We now provide numerical evidence supporting some of the conclusions of Section III. The data is taken from [11], where the reader will find additional numerical tests along with a discussion of the generalized baker maps, the test systems used to obtain numerical data in this and the following section. The baker maps are a class of Bernoulli systems and a paradigm of hard chaotic behavior. A symbolic dynamics allows one to easily identify the locations of the periodic orbits and to find their exponents. Furthermore, the local dynamics of these systems around any periodic orbit is exceedingly simple, the stable and unstable manifolds always being oriented along the p and q directions, in accordance with Eq. 6. Several system parameters can be easily varied to collect wavefunction statistics while keeping fixed the linearized dynamics near a given periodic orbit. Semiclassical spectra and eigenstates can be efficiently computed, allowing for comparison between these and the exact quantum stationary properties [40].

In Fig. 1a appears a typical local line spectrum $S(E)$ (Eq. 1) for a wavepacket centered on a periodic orbit with exponent $\lambda = 0.79$. A total of 223 states exist in the energy interval $[-\pi, \pi]$; a portion of this spectrum containing the peak of the linearized envelope $S_{\rm lin}(E)$ (dotted line) is shown in the figure. Two intermediate envelopes, defined by cutting off the sum in Eq. 18 at $T = 30$ (a time long compared to the orbit period but short compared to the Heisenberg time) also appear in the figure. The solid curve is obtained from the exact

quantum calculation until $|T| < 30$, while the dashed curve comes from the corresponding semiclassical calculation. We see that the large wavefunction intensities do appear in the energy region predicted by the linear envelope, and further refinement of the spectrum is obtained from intermediate-time dynamics.

In Fig. 1b we again zoom in on the energy region in which the linearized envelope (now shown as a solid line) is peaked. The full spectrum $S(E)$ is still marked by the vertical solid lines, while a semiclassical line spectrum appears as dashed lines. Though the quantum and semiclassical spectra differ in their detailed properties, they are both observed to fluctuate around the same linear envelope $S_{\rm lin}$. In Fig. 1c we separate out these random fluctuations in the quantum spectrum from the short-time constraint $S_{\rm lin}$, by dividing through all of the line heights by $S_{\rm lin}$. We see that the rescaled line heights display energy-independent oscillations, equally strong near the peak and valley of the envelope.

In [11] the rescaled line heights of Fig. 1c are collected for an ensemble of systems, and compared to the Porter-Thomas prediction of Gaussian random fluctuations. Because we will be focusing on wavefunction intensities in the following section, we omit this data here, but will point out that the IPR for the spectrum of Fig. 1 is 7.93, which agrees well with the scar theory prediction 7.94 for this value of λ when the random fluctuation factor $F = 2$ is included (see Eq. 23). The IPR of the semiclassically evaluated spectrum for this system is 8.46.

In Fig. 2 we plot the numerically obtained values of the IPR for a large number of systems, with the test wavepacket placed on orbits of varying exponent λ ($0.28 < \lambda < 1.94$). The actual value of the IPR is plotted versus the linear IPR prediction, $< S_{\rm lin}^2 >$, i.e. the amount of fluctuation in the linear envelope. The latter is obtained as in Eq. 23 by summing linearized return probabilities for a wavepacket centered on an orbit of exponent λ. Three sets of data points are shown in the figure (see [11]), and a line of slope $F = 2$ is plotted for comparison. The data is consistent with the IPR being given by a product of the fluctuations in the linearized envelope itself with Porter-Thomas fluctuations under the envelope. The spread of data points in the figure is also consistent with $O(1/\sqrt{N_{\rm eff}})$ fluctuations in the IPR from system to system, where $N_{\rm eff}$ is the effective number of states under the linearized envelope [11].

In Fig. 3 we plot the 2-point correlation function $< S(E + \Delta E)S(E) > / < S(E) >^2$ of the spectrum shown in Fig. 1a (plusses). In the same figure is plotted (with diamonds) the 2-point correlation function of the rescaled spectrum of Fig. 3c. Again, we see that all of the non-random structure in the spectrum arises from the presence of the linearized envelope $S_{\rm lin}$, and that the rescaled spectral lines are completely uncorrelated.

V. WAVEFUNCTION INTENSITY STATISTICS

As an example of the calculations which can be easily performed within the framework of scar theory, we discuss the tail of the wavefunction intensity distribution, and its deviations from the exponential tail of RMT [12]. This quantity has been analyzed previously for disordered systems, where a log-normal tail is predicted [41] and observed [42]. That analysis applies to scatterers that are small compared to the Fermi wavelength of the system. In the semiclassical limit, where the scatterer size is kept fixed while the wavelength is taken to zero, one obtains very different behavior, as we shall see below. This suggests that although RMT is known to be a good zeroth-order approximation for both quantum chaotic and diffusive behavior, the corrections to RMT may be qualitatively very different in the two kinds of systems.

As we saw above in Section III, individual spectral lines in the local density of states $S(E)$ show, in the semiclassical limit, chi-squared (Porter-Thomas) fluctuations around the linear envelope $S_{\rm lin}$. For complex eigenstates (in the absence of time-reversal symmetry) the chi-squared distribution has two degrees of freedom, and without scarring effects the probability of having a spectral line height greater than x is given by $P(x) = \exp(-x)$. Here the intensity x is normalized to have a mean value of unity, i.e. $x_n = N|\langle n|a^{q_0,p_0}\rangle|^2$, where $|a^{q_0,p_0}\rangle$ is the Gaussian wavepacket and N is the total number of states ($N = 1/h$ for a classical phase space area of unity). Including scarring effects for an orbit of instability exponent λ, this distribution is modified to

$$P(q_0, p_0, \sigma, \lambda, E, x) = \exp\left(-x/S_{\rm lin}(q_0, p_0, \sigma, \lambda, E)\right) \quad (28)$$

for a eigenstate with energy E overlapping with a Gaussian centered at (q_0, p_0) with width σ. Thus, the average intensity becomes $S_{\rm lin}(q_0, p_0, \sigma, \lambda, E)$, and the entire distribution is stretched out by this factor. Now we perform an energy average, remembering that for a map the quasi-energy E is defined to lie between 0 and 2π only. We notice that the tail of the intensity distribution will be dominated by the peak of the spectral envelope at the EBK quantization energy $E = \phi$. Without loss of generality we may set $\phi = 0$, and perform the energy integral using the saddle point approximation around $E = 0$, where $S_{\rm lin}$ is maximized. We then obtain

$$\begin{aligned} P(q_0, p_0, \sigma, \lambda, x) &= \frac{1}{2\pi}\int dE P(q_0, p_0, \sigma, \lambda, E, x) \\ &\approx \frac{1}{\sqrt{2\pi}} \frac{\exp(-x/S_{\rm lin}(q, p, \sigma, \lambda, E=0))}{\sqrt{\frac{-x}{S_{\rm lin}(0)^2}\frac{\partial^2 S_{\rm lin}}{\partial E^2}}}\,, \end{aligned} \quad (29)$$

valid in the limit of large x. For small λ, the sum over time steps can be replaced by an integral, and we have at $q_0 = p_0 = 0$

$$S_{\rm lin}(E) = \int dt \frac{e^{-iEt}}{\sqrt{\cosh \lambda t}}\,. \quad (30)$$

Now by dimensional analysis, $S_{\rm lin}(0) = Q/\lambda$ and $\frac{\partial^2 S_{\rm lin}}{\partial E^2}(0) = -W/\lambda^3$, where Q and W are numerical constants. We thus obtain the $\hbar-$*independent* tail of the intensity distribution for a wavepacket centered on a periodic orbit,

$$P(q_0 = 0, p_0 = 0, \sigma, \lambda, x) = \frac{1}{\sqrt{2\pi}} \frac{Q}{\sqrt{W}} \lambda (x\lambda)^{-1/2} e^{-x\lambda/Q} \,. \tag{31}$$

This is the total probability of having a wavefunction intensity enhanced by a factor x over the average intensity, on a periodic orbit of instability exponent λ. The result is independent of σ, and thus of the aspect ratio of the test state in phase space. Notice that the exponential tail has been effectively stretched by a factor of Q/λ, corresponding to the height of the peak of the linear envelope at small λ. There is also a linear suppression factor of λ, corresponding to the energy width of the peak in $S_{\rm lin}(E)$, and indicating that only a fraction scaling as λ of all the eigenstates are effectively scarred. See the upper curve in Fig. 4 for a comparison of this result with numerical data.

The region of validity of Eq. 31 is

$$1 \ll \lambda^{-1} \ll x \ll N \,. \tag{32}$$

The first inequality ensures that many iterations of the periodic orbit contribute (so the sum over iterations can be replaced by an integral) and the scarring is strong. In fact, however, because of the large value of the numerical constant $Q \approx 5.24$, the formula works well even for exponents as large as $\log 2$, as will be seen in the numerical study below. The second inequality says that we are in the tail of the distribution and the events are all coming from the peak of the linear envelope $S_{\rm lin}$. The third inequality is a unitarity constraint: obviously our assumption of random fluctuations breaks down for intensities of order N, when the entire wavefunction would be concentrated in a phase space area of order $\hbar$.

A similar analysis can be performed integrating over the phase space variables q_0 and p_0, to obtain the full distribution of wavefunction intensities everywhere in phase space. The exponential $\exp\left(-x/S_{\rm lin}(q_0, p_0, \ldots)\right)$ must now be expanded to second order in q_0, p_0 around the maximum $q_0 = p_0 = 0$. Then upon integration by the saddle point method we obtain a determinant factor [12] of $\frac{\pi\hbar}{(x\lambda)} \frac{Q^2}{Z}$, again independent of σ. Z is another numerical constant, related to the falloff of $S_{\rm lin}$ away from the fixed point $q_0 = p_0 = 0$. The factor of $\hbar$ in front results from the fact that the dominant contribution to the tail comes from a region scaling as $\hbar$ surrounding the periodic orbit (compare Eq. 27 and the discussion following). Combining this determinant prefactor with the expression in Eq. 31, we obtain the tail of the distribution of overlap intensities after energy and phase space averaging,

$$P(\lambda, x) = \sqrt{\frac{\pi}{2}} \frac{Q^3}{Z\sqrt{W}} \hbar \lambda (x\lambda)^{-3/2} \exp\left(-x\lambda/Q\right) . \tag{33}$$

This result is valid in the regime

$$\max(\log N, \lambda^{-1}) \ll x \ll N \,. \tag{34}$$

Here $\log N$ is the value of intesnity x near which the RMT exponential decay law $\exp(-x)$ reaches values of order $\hbar = 1/2\pi N$. Near this value of x, a crossover occurs between the head of the distribution, which is dominated by non-scarred region of phase space and approaches the Porter-Thomas (RMT) prediction, and the tail, dominated by scarring, given by the expression above. The expression Eq. 33 holds also for an ensemble of systems, all having one orbit with instability λ. In principle, we should of course do a sum over all periodic orbits in a given system, however the tail will clearly always be dominated by the orbit with smallest λ. Numerical data confirming Eq. 33 appears in the lower curve of Fig. 4.

Finally, we consider an ensemble of systems where the value of the smallest exponent λ varies from realization to realization, with distribution $\mathcal{P}(\lambda) = C\lambda^\alpha$ for small λ. An example would be a billiard system with many movable disks, each of diameter much larger than the wavelength. Then using Eq. 33 and integrating over λ we obtain

$$P(x) = C\sqrt{\frac{\pi}{2}} \frac{Q^3}{Z\sqrt{W}} Q^{\alpha+1/2} \Gamma(\alpha + 1/2) \hbar x^{-(2+\alpha)} \,. \tag{35}$$

Note that this is an uncontrolled approximation because we have integrated over λ after having assumed $x\lambda$ to be large. However, if we had included higher-order corrections in $(x\lambda)^{-1}$ in Eq. 33, the scaling of $P(x)$ would remain unchanged, i.e.

$$P(x) = Cf(\alpha) \hbar x^{-(2+\alpha)} \,, \tag{36}$$

with the dimensionless function $f(\alpha)$ somewhat different from that given in Eq. 35. The important point is that the tail displays power-law behavior in the intensity x, a strong deviation from the exponential prediction of RMT. As with Eq. 33, this asymptotic form is valid for values of x large compared to $\log N$ and small compared to N. For small x we again expect a crossover to the Porter-Thomas form $\exp(-x)$. For large x we expect a downward correction away from the $x^{-(2+\alpha)}$ form, with a breakdown of the approximation occurring at some fraction of N, depending on α.

We now present numerical evidence for the results of this section, using the same ensemble of systems as in the numerical tests of the previous section. The data shown here was originally obtained in [12]. In Fig. 4 we fix the instability exponent λ of the least unstable periodic orbit at $\log 2$, and obtain a cumulative wavefunction intensity distribution for a wavepacket centered on the orbit (upper thick curve), and a combined distribution for wavepackets randomly located over the entire phase

space (lower thick curve). The tails of the distributions compare well with the scar theory predictions of Eq. 31 (dashed curve) and Eq. 33 (solid curve). Notice that the generic wavepacket wavefunction intensity distribution (lower thick curve) rolls over to the RMT prediction (dotted line) at small values of the intensity. The log-time in this system, near which value of x the crossover is expected to occur is $T_{\log} \approx 7$.

In Fig. 5 the same distribution is shown after ensemble averaging over systems with classical orbits of different instability exponents. We see that at small values of x the data agrees well with the RMT prediction (dashed line), while the tail follows the power-law behavior of Eq. 35 (solid line).

VI. IMPROVED (UNIVERSAL) MEASURES OF SCARRING

We have noted previously an ambiguity in the choice of Gaussian wavepacket to serve as a test state for measuring scarring effects. Even after requiring that the wavepacket be optimally oriented relative to the invariant manifold directions, a one-parameter family of possible Gaussians remains, parametrized by the aspect ratio σ^2 (See Eq. 7). Together, these fill a hyperbolic region $|qp| \leq O(\hbar)$ encompassing the stable and unstable axes: the scarring phenomenon is present in this entire region and not just at the periodic orbit $q = p = 0$ itself. [Compare this with the hyperbolic fringes in the Wigner spectral function obtained by Berry [27]]. This fact suggests that the Husimi-space ambiguity may be resolved, and a better measure of scarring obtained, by including information about wavefunction behavior in this entire hyperbolic region instead of choosing one Gaussian of arbitrary width σ.

A similar ambiguity arises when we consider a higher-period orbit of a map, or a periodic orbit of a continuous-time system. There, the test wavepacket is chosen to be centered at one of the many possible periodic points; again a less arbitrary measure of scarring should be obtainable by considering the wavefunction along the entire orbit.

The obvious way to resolve these ambiguities is by averaging scarring intensity over wavepackets of different aspect ratios in phase space, or over wavepackets centered at different periodic points, or both. Thus, we replace the single wavepacket $|a\rangle$ by a density operator ρ, and define the scarring strength for a given eigenstate $|n\rangle$ as

$$I_{n\rho} \equiv \langle n|\rho|n\rangle \,. \tag{37}$$

Then we can construct a wavepacket-averaged local density of states analogous to Eq. 1:

$$S_\rho(E) = \sum_n I_{n\rho}\delta(E - E_n) \,, \tag{38}$$

and a corresponding inverse participation ratio

$$\mathrm{IPR}_\rho = N \sum_n I_{n\rho}^2 \,. \tag{39}$$

To obtain averaging over the wavepacket aspect ratio at a given periodic point, we write

$$\rho = \mathcal{N} \int dt\, e^{-t^2/T_0^2}\, |a_{\sigma e^{\lambda t}}\rangle\langle a_{\sigma e^{\lambda t}}| \,. \tag{40}$$

The exponent λ can be chosen to be the instability exponent of the unstable orbit (Eq. 6), but this choice is in fact arbitrary, and λ can be reabsorbed into the overall normalization factor $\mathcal{N}$ and the time cutoff T_0. In the absence of the cutoff T_0, the hyperbolic test state would be completely scale invariant, giving equal weight to Gaussians of all aspect ratios, from tall and thin to short and wide. The cutoff is, however, necessary because the linearized dynamics of Eq. 6 is in fact only valid in a finite classical region around the periodic orbit (and also it eliminates possible normalization difficulties). To get an optimal measure of scarring, we choose the initial width σ such that the wavepacket has the same aspect ratio in phase space as the linearizable region surrounding the orbit in which the equations of motion are well described by Eq. 6. Then the initial wavepacket $|a_\sigma\rangle$ can expand by the same stretching factor along either of the two invariant directions before hitting the "edge" of the linearizable region. One easily sees that if A is the phase-space area of the linearizable region, we want to choose

$$T_0 = \frac{c}{2\lambda} \log \frac{A}{4\hbar} \,. \tag{41}$$

c is an arbitrary constant of order unity: it determines the exact suppression factor in Eq. 40 for a Gaussian just touching the boundary of the linearizable region. In the semiclassical limit, of course, $A \gg \hbar$, and the precise size A of the region needs to be determined only to within a multiplicative factor; it may indeed in this limit be taken as equal to the volume of the entire accessible phase space. Notice that up to a constant, T_0 has the same form as the log-time $T_{\log}$ defined in Section III. The Gaussian form of Eq. 40 in the time variable t is somewhat arbitrary, and also not important in the $\hbar \to 0$ limit. See [13] for a fuller discussion.

To average over the position of the periodic point, we similarly may define a phase-space "tube"

$$\rho = \mathcal{N} \int dz\, |a_{z,\sigma,\sigma_z}\rangle\langle a_{z,\sigma,\sigma_z}| \,, \tag{42}$$

where the z coordinate parametrizes the periodic orbit in phase space, and at each periodic point the wavepacket is chosen to have width σ_z along the direction of the orbit and width σ in the unstable direction at that point on the orbit. We recall that the Husimi function is nothing other than a Gaussian smoothing of the Wigner spectral

function; thus averaging the Husimi function around the periodic orbit coincides with the phase-space tube averaging of Fishman, Agam, et al. [29]. In [29], the Gaussian width σ is generally taken to be fixed as one goes around the tube; however that is a coordinate-dependent condition, and in general one may take σ to be an arbitrary function of z.

More generally one can, of course, combine the averaging procedures of Eqs. 40,42, to obtain a fully-universal measure of scarring. In the strong-scarring limit $\lambda \ll 1$ one may also without loss of generality begin with one wavepacket only and allow the dynamics itself to generate the density matrix ρ:

$$\rho_{\rm dyn} = \sum_{t=-\infty}^{+\infty} e^{-t^2/T_P^2 T_0^2} \, |a_{\rm lin}(t)\rangle\langle a_{\rm lin}(t)| \, . \tag{43}$$

Here $|a_{\rm lin}(t)\rangle$ is the original Gaussian $|a\rangle$ evolved in accordance with the *linearized* dynamics: for example, if t is an integer multiple of the period T_P, then $|a_{\rm lin}(t)\rangle$ is centered at the same periodic point as $|a\rangle$, but with width $\sigma \to \sigma e^{\lambda t/T_P}$. T_0 is defined as before (Eq. 41), using the full instability exponent λ for one iteration of the *entire* primitive orbit. λ/P is the exponent *per time step*; hence the factor of T_P^2 in Eq. 43.

To understand what gains may be achieved by the averaging process described here, we need to consider correlations in the local density of states between different wavepackets placed on the same periodic orbit. Indeed, these correlations will also be very important when we discuss conductances and phase space transport in Section VII. To begin, consider two wavepackets $|a\rangle$ and $|b\rangle$ and their overlap intensities I_{na}, I_{nb} with the eigenstates $|a\rangle$ of the system. We may define a long-time averaged transport probability P_{ab} [6] as

$$P_{ab} = \lim_{T\to\infty} \frac{1}{T} \sum_{t=0}^{T-1} |\langle a|U^t|b\rangle|^2 \, . \tag{44}$$

For a nondegenerate spectrum we easily see

$$P_{ab} = \sum_n |\langle a|n\rangle|^2 \, |\langle b|n\rangle|^2 = \sum_n I_{na} I_{nb} \, . \tag{45}$$

In particular, the IPR corresponds to the special case

$$\mathrm{IPR}_a = N P_{aa} = N \sum_n I_{na}^2 \, . \tag{46}$$

The P_{ab} can be thought of as the covariance matrix of the local densities of states for different wavepackets, with P_{aa} being the variances or diagonal matrix elements; the correlation between two local densities of states is then given by

$$C_{ab} = \frac{P_{ab}}{\sqrt{P_{aa} P_{bb}}} \, . \tag{47}$$

Consider first the case where $|a\rangle$ and $|b\rangle$ are exact time iterates of one another: $|b\rangle = |a(t)\rangle$ for some time t. Then the two local densities of states are identical,

$$P_{ab} = P_{aa} = P_{bb} = \frac{F}{N} g(\lambda) \tag{48}$$

and the correlation is unity. $g(\lambda) \approx \pi/\lambda$ for small λ is the scarring IPR enhancement factor (Eq. 23). On the other hand, if we consider two wavepackets that have the same short-time behavior but are otherwise unrelated (e.g. if $|a\rangle$ and $|b\rangle$ are located on different periodic orbits of the same length and instability exponent λ), then the two have the same linearized spectral envelope but independent fluctuations under that envelope. Then

$$\begin{aligned} P_{aa} &= P_{bb} = \frac{F}{N} g(\lambda) \\ P_{ab} &= \frac{1}{N} g(\lambda) \\ C_{ab} &= \frac{1}{F} \, . \end{aligned} \tag{49}$$

The correlation in this case is of order unity but still less than one.

In the intermediate case, we may have two wavepackets one of which *partly* overlaps the other under short time evolution. Then the random spectral fluctuations under the two identical envelopes are partially correlated, and we get a correlation $1/F < C_{ab} < 1$ [13]. However, for small λ, *any* two wavepackets optimally oriented along the same periodic orbit (whether centered at the same periodic point or not) will overlap each other with a very large amplitude under time evolution. The reason is that the wavepacket stretches very little each orbit iteration, and there will always be some n for which $\sigma e^{n\lambda}$ is very close to any chosen width σ'. Expressions for determining the LDOS correlation C_{ab} given λ and the relative widths of the two wavepackets are given in [13], where the predictions are also numerically tested [Fig. 6]. It is found that a scarring enhancement factor $g(\lambda)$ of 2 (corresponding to instability exponent $\lambda \approx \log 5$), is already associated with a *minimum* correlation of 0.99 between the least correlated wavepackets on such an orbit. Orbits that have smaller λ and are thus more scarred have correlations C_{ab} even closer to unity.

In Fig. 6 we plot the predicted and numerically observed correlations C_{ab} between local densities of states for two wavepackets centered on the same periodic orbit. The parameter z is defined such that wavepacket $|a\rangle$, under linear evolution, evolves to be centered at the same point as $|b\rangle$, but with width $e^{\lambda(n+z)}$ times that of $|b\rangle$, where n is an arbitrary integer. For integer z the two local densities of states are the same, and the correlation is unity. The smallest correlation is obtained for half-integer z. The upper and lower curves in the figure correspond to instability exponents $\lambda = \log 5$ and $\lambda = \log 10$, respectively. The data is obtained by averaging over an ensemble of kicked-baker maps [13], and the theoretical

curves are obtained from [13]. We notice that even for these very moderate instability exponents, the minimum value of C_{ab} for the most uncorrelated wavepackets is already very close to one. The correlations get even closer to one as λ decreases.

Thus in the strong scarring limit $\lambda \ll 1$, there is in fact no ambiguity in choosing either the central point z or the aspect ratio σ^2 of the test Gaussian on a periodic orbit. This also means that the density matrix averaging outlined above *does not* produce a scarring measure different from that given by any one arbitrary wavepacket along the orbit.

Yet it is possible to use our knowledge of the entire orbit and the linearized classical dynamics surrounding it to build an improved scarring test state. Beginning once again with a fixed point of a discrete-time map, we construct the *coherent* sum

$$\Psi = \mathcal{N} \int dt\, e^{-t^2/T_0^2} e^{i\theta t} \, |a_{\sigma e^{\lambda t}}\rangle \tag{50}$$

(compare with Eq. 40). Again, T_0 is a cutoff time (Eq. 41) for the linearized dynamics, and $\mathcal{N}$ is a normalization constant. θ is an arbitrary phase accumulated per time step. We notice that if the linear equations of motion (Eq. 6) were exact, we could remove the cutoff T_0, and the state Ψ would be an exact eigenstate of the dynamics, with energy $\phi + \theta$. The extent to which Ψ fails to be an exact eigenstate is determined by the nonlinear nature of the dynamics beyond the log-time $T_0 \sim |\log \hbar|/\lambda$, whereas the failure of a single wavepacket $|a\rangle$ to be an eigenstate results already from the initial decay at the time scale $1/\lambda$. Just as scarring strengths and IPR's for a single wavepacket scale as $1/\lambda$ because the autocorrelation function $A_{\rm lin}$ remains of order unity for the first $O(1/\lambda)$ iterations of the orbit, so here the autocorrelation function should decay on a time scale of order $T_0 \sim |\log \hbar|/\lambda$ in the $\hbar \to 0$ limit, and scarring strengths should scale likewise.

Indeed, in the strong-scarring semiclassical regime ($\lambda \to 0$ and $\hbar \to 0$) we obtain [13] the short-time autocorrelation function for Ψ

$$A^{\Psi}_{\rm lin}(t) = e^{-i(\phi+\theta)t} e^{-t^2/T_0^2} \, . \tag{51}$$

Fourier transforming, we then have the spectral envelope

$$S^{\Psi}_{\rm lin}(E) = \sqrt{2\pi} T_0 e^{-(E-\phi-\theta)^2 T_0^2/2} \, , \tag{52}$$

centered at energy $E = \phi + \theta$, with width scaling as $\lambda/|\log \hbar|$, and height and IPR [Fig. 7] scaling as $|\log \hbar|/\lambda$. In particular, the inverse particpiation ratio has the following asymptotic form for small λ and small $\hbar$:

$$\mathrm{IPR}_{\Psi} = F \sqrt{\pi} T_0 \, . \tag{53}$$

Note that the LDOS of a single wavepacket is always peaked at the "quantization energy" $E = \phi$, whereas by taking coherent superpositions we may construct an "off-resonance" state with a LDOS peaked away from this energy [see Fig. 8]. For $\theta = 0$, the state Ψ lives on the fixed point itself and on the invariant manifolds within the linearizable region around the orbit; for nonzero θ it lives on hyperbolic regions asymptotic to the two manifolds [Fig. 9]:

$$\frac{qp}{\hbar} \sim \theta/\lambda \tag{54}$$

These hyperbolic structures living near the periodic orbits but not on the orbits themselves have been studied previously by Nonnenmacher and Voros [35], and observed before that by Saraceno [36] and by O'Connor and Tomsovic [37] in the context of the baker map. The association between energy shifts and hyperbolic structures surrounding the orbit is also evident in the phase of the dynamics in Eq. 27 for wavepackets centered off of the periodic orbit. We see there that at times short compared to λ^{-1}, the phase accumulated per time step is shifted by the amount $q_0 p_0 \lambda/\hbar$ (where (q_0, p_0) is the center of the wavepacket), and the peak of the spectral envelope in quasienergy space must therefore also be shifted by an amount of this order.

The scarring measure given by Eq. 50 may truly be said to be universal and optimal, as it eliminates the ambiguity inherent in the Husimi space measure, and fully incorporates all knowledge not only about the location of the periodic orbit itself but also about the linearized dynamics around this orbit. We note here that the expressions Eqs. 51,52 are valid in the $\lambda \to 0$ limit, where scarring is strong. However, this improved measure of scarring can also be used for moderate λ, where the expressions (Eq. 51,52) need to be modified. Although the dependence of the spectral envelope on λ is more complicated away from the $\lambda \ll 1$ regime, the spectral envelope height and the IPR still scale as $\log \hbar$ in the semiclassical limit, for arbitrary λ. Thus, even an unstable orbit with moderate or large instability exponent, which will be rather weakly scarred using the usual Gaussian wavepacket measure, will always be strongly scarred using the "universal scarmometer" Ψ, in the $\hbar \to 0$ limit. See [13] for a more thorough discussion of this point, as well as of finite $\hbar$ corrections to theoretical predictions of scar strength.

We now briefly discuss the extension of the above methods to longer periodic orbits of maps and to continuous time. Here, even greater enhancement of scarring intensity is obtained because the universal test state Ψ is naturally defined to live along the *entire* orbit. For a map of period T_P, we recall that there are T_P optimal energies

$$E_k = \frac{\phi + 2\pi k}{T_P} \quad , \quad k = 0 \ldots T_P - 1 \, . \tag{55}$$

that "quantize" the orbit in the EBK sense. The spectral envelope of a single Gaussian wavepacket will be peaked at all these T_P energies (see the discussion following Eq. 24). We now choose one such quantization

energy and construct an optimal scarring test state Ψ centered at energy $E_k + \theta/T_P$:

$$\Psi = \mathcal{N} \sum_p \int dt e^{-t^2/T_P^2 T_0^2} \times e^{i(E_k+\theta/T_P)p + i\theta t/T_P - i\phi_p} |a_{x_p, \sigma f_p e^{\lambda t/T_P}}\rangle \,. \quad (56)$$

Here f_p is a stretching factor, and ϕ_p is a phase, both defined by

$$U^p_{\rm lin} |a_{x_0,\sigma}\rangle = e^{-i\phi_p} |a_{x_p, \sigma f_p e^{\lambda_p/T_P}}\rangle \,. \quad (57)$$

f_p and ϕ_p take into account the fact that stretching and phase accumulation along the orbit may both be non-uniform; of course, $f_{T_P} = 1$ and $\phi_{T_P} = \phi$. The correct phases ϕ_p are particularly crucial for getting constructive interference between different periodic points. Once again, θ is an arbitrary off-resonance parameter. For $\theta = 0$, the test state lives on all T_P periodic points and their invariant manifolds; for $\theta = O(\lambda)$, the test state occupies hyperbolic regions $qp \sim \hbar$ near these same periodic points.

The short-time autocorrelation function and the spectral envelope take the same form as in the $T_P = 1$ fixed point case, making the substitutions

$$T_0 \to T_0 T_P \;,\; \lambda \to \lambda/T_P \;,\; \theta \to \theta/T_P \;,\; \phi \to E_k \quad (58)$$

throughout. Notice in particular that the relevant instability parameter is λ/T_P, the exponent *per time step*, and not the exponent λ per iteration of the entire orbit which governs the strength of the single-wavepacket scarring measure. In particular, the peak height in the LDOS $S^\Psi_{\rm lin}(E)$ and the corresponding IPR both scale as $(\lambda/T_P)^{-1} |\log\hbar|$ for small λ/T_P. Thus, as long as the Lyapunov exponent λ/T_P remains small, the effects of longer orbits (up to the mixing time) can remain strong using the Ψ test-state measure, whereas the single-wavepacket measure will fail to detect a strong signal from these longer orbits. For $T_P > 1$, a dramatic increase in scarring strength is observed even for moderate $\hbar$, because of this additional T_P factor.

For small λ, the optimal test state Ψ can also be generated dynamically:

$$\Psi_{\rm dyn} \sim \sum_t e^{-t^2/T_P^2 T_0^2} \, e^{i(E_k+\theta/T_P)t} |a_{\rm lin}(t)\rangle \quad (59)$$

(compare Eq. 43). Here $|a\rangle$ is a wavepacket of width σ centered at *any* point along the periodic orbit.

The expressions Eqs. 56,59 also generalize in an obvious way to continuous time [13]. Again, one chooses any energy E_k which quantizes the action in units of $\hbar$, and an arbitrary energy offset $\hbar\theta/T_P$ if one wishes to measure off-resonance scars. The short-time autocorrelation function again decays on the time scale $T_0 T_P \sim T_P \lambda^{-1} \log A/\hbar$. In the energy domain it produces a *single* peak of height scaling as $(T_P \log A/\hbar)/\lambda$ compared to the background spectral envelope (of width $\hbar/T_{\rm free}$, see discussion in Section III) which enforces energy conservation. This is to be compared with the ordinary scarring envelope which has peaks at *all* of the quantization energies with height scaling simply as $1/\lambda$. Once again, we find that longer orbits can be detected as easily as short ones using the improved scarring measure[3] and an additional logarithmic scarring enhancement factor is obtained in the semiclassical limit.

We mention here the closely related work of de Polavieja, Borondo, and Benito on improved measures of scarring in Hamiltonian systems [30] and of Simonotti, Vergini, and Saraceno [24] on the surface of section in a billiard system. In both cases, a coherent superposition of wavepackets is used to construct a better test state for measuring scarring effects. However, both these groups consider only one (arbitrarily shaped) wavepacket at each periodic point of the orbit; thus they obtain the enhancement factor T_P but not the extra $|\log\hbar|$ factor that comes from using the linearized dynamics to fill the entire hyperbolic region surrounding the orbit. See [13] for a fuller discussion of this and other related issues.

Numerical data in this section is obtained from an ensemble of kicked baker maps; see [13] for details. In Fig. 7, we show the IPR plotted as a function of the cutoff constant c (see Eq. 41), for various values of the system size N ($N = 1/h$ is the number of Planck-sized cells in the classical phase space). Here the instability exponent for the period-one orbit is $\lambda = |\log 0.18|$. The upper dashed curve is the $N \to \infty$ theoretical prediction, which converges to the asymptotic form of Eq. 53 (lower dashed line) for large T_0 (i.e. for exponentially small $\hbar$, keeping fixed the cutoff parameter c). The linearized theory is expected to start breaking down for $c \geq 1$ (the rightmost six points on each data curve).

In Fig. 8 are shown the smoothed (numerically obtained) local densities of states for off-resonance test states Ψ, for several off-resonance angles θ. The tallest peak corresponds to the on-resonance test state $\theta = 0$; in the $\hbar \to 0$ limit the peaks would all be the same height and shape. The system size here is fixed at $N = 800$, the cutoff parameter is $c = 0.6$, and once again $\lambda = |\log 0.18|$. In Fig. 9 are displayed Husimi plots of the universal test state Ψ for (a) $\theta/\lambda = 0.8$ and (b) $\theta/\lambda = 2.5$. For $\theta = 0$ (not shown), Ψ lives entirely on the orbit (located here in the center of the figure) and on the invariant manifolds (vertical and horizontal lines intersecting at the center of the figure). As θ becomes non-zero, Ψ moves off of the manifolds and onto hyperbolic regions asymptotic to the manifolds (Eq. 54). Choosing the opposite sign for

[3] Of course, given a value of $\hbar$ only orbits of period less than the mixing time for that $\hbar$ can be profitably studied; our approach is based on the assumption $T_P < T_{\log}$, so that linearized dynamics remains valid over several iterations of the orbit.

θ would produce a test state occupying the other two quadrants.

Finally, in Fig. 10 we show a numerically obtained, smoothed spectrum for a wavepacket placed on a period-2 orbit (double-peaked solid curve), and for the universal test state Ψ constructed on the same orbit (tall single peak). These agree well with the theoretical predictions (dashed curves) based on the linearized dynamics near the periodic orbit, which has a total exponent $\lambda = |\log 0.168|$ over the two-step period. One of two possible on-resonance energies has been chosen for the test state Ψ, which is again constructed using cutoff constant $c = 0.6$. The enhancement here is more dramatic than for the period-one orbits, due to the fact that universal scarring strength depends only on the exponent per unit time along the orbit, not on the orbit length itself.

VII. OPEN SYSTEMS: SCARS AND ANTISCARS

We now proceed to consider the last major topic to be covered in this review: the effect of unstable periodic orbits on weakly open systems, where experimentally accessible quantities such as resonance peaks and conductance curves can be measured. See [14] for a more detailed exposition of the effect of periodic orbits on resonances and on the probability to remain in an open quantum chaotic system. A study of conductance curves in two-lead chaotic systems is now in progress [15].

Let H_0 be a quantum Hamiltonian for a classically chaotic (closed) system, and consider adding a small opening to the system, through which probability can escape. If the opening size corresponds to less than one open channel, so that quantum resonances will be non-overlapping, we can write an effective Hamiltonian for the open system:

$$H = H_0 - i\frac{\Gamma}{2}|a\rangle\langle a|\,. \tag{60}$$

Here $|a\rangle$ is a quantum channel associated with the opening, and Γ is the decay rate in that channel. $|a\rangle$ could be a Gaussian wavepacket at the location of the hole, or a position or momentum state. The main effect of the opening on a wavefunction $|n\rangle$ of the closed system is that it acquires a decay width proportional to the intensity of the wavefunction at the opening:

$$\Gamma_n = \Gamma|\langle n|a\rangle|^2\,. \tag{61}$$

In RMT, the intensities $x_n \equiv N|\langle n|a\rangle|^2$ follow a chi-squared distribution: $P(x) = \frac{1}{\sqrt{2\pi x}}\exp(-x/2)$ for real overlaps, and $P(x) = \exp(-x)$ if the overlaps $\langle n|a\rangle$ are complex. On the other hand, if the decay channel $|a\rangle$ happens to be located on a short periodic orbit, we know that the distribution of decay rates is stretched by the factor $S^a_{\rm lin}(E)$, this being the smoothed LDOS at $|a\rangle$. [Compare with the discussion of wavefunction intensity statistics in Section V.] This will have a profound effect on the distribution of resonance lifetimes in the system. Near the would-be EBK quantization energies where $S_{\rm lin} > 1$, resonance lifetimes are decreased (by a factor scaling as λ^{-1} for small λ), while far from these energies resonances tend to be narrow compared with the expectations of RMT. In order to have a concrete quantity to focus on, let us consider the ensemble-averaged probability to remain in the system at long times. This quantity has been investigated previously for disordered systems [43], and a log-normal long-time tail was found. We investigate here what deviations from RMT predictions can be obtained as a result of periodic orbit effects.

First consider the RMT case, with complex eigenstates. Because mixing between the states of the closed system can be neglected in the small Γ regime, the total probability to remain in the system is given by a sum over these states:

$$\begin{aligned} P_{\rm rem}(t) &= \frac{1}{N}\sum_{n=0}^{N-1} e^{-\frac{x_n}{N}\Gamma t} = \int_0^\infty dx P(x) e^{-x\Gamma t/N} \\ &= \int_0^\infty dx e^{-x} e^{-x\Gamma t/N} = \frac{1}{1+\Gamma t/N}\,. \end{aligned} \tag{62}$$

Here N is the total number of states in the system; the classical decay rate is given by

$$\Gamma_{\rm cl} = \Gamma/N \tag{63}$$

because only one channel has the possibility to decay. We see that at short times ($t \ll \Gamma_{\rm cl}^{-1}$), the probability to remain in the system is $P_{\rm rem}(t) \approx 1 - \Gamma_{\rm cl} t$, as expected, while at long times the power-law asymptotic behavior

$$P_{\rm rem}(t) \approx \frac{1}{\Gamma_{\rm cl} t}\,. \tag{64}$$

is obtained. The analysis can be extended to $M > 1$ open channels, where the power of the long-time behavior scales with M. Notice that at the classical level we expect an exponential decay law $P_{\rm rem}(t) = \exp(-\Gamma_{\rm cl} t)$, since the system is chaotic and the hole small enough that the probability distribution inside the system never deviates from uniformity (the mixing time being very short compared to the decay time).

Now take the open channel $|a\rangle$ to be centered on an unstable periodic orbit of exponent λ. The intensities are then distributed in each energy range as a chi-squared distribution with mean $S_{\rm lin}(E)$:

$$P(x) = \frac{1}{S_{\rm lin}(E)} e^{-x/S_{\rm lin}(E)}\,. \tag{65}$$

Then the probability to remain at long times is given by

$$\begin{aligned} P_{\rm rem}(t) &= \int_0^\infty dx P(x) e^{-x\Gamma t/N} = \frac{1}{1 + S_{\rm lin}(E)\Gamma t/N} \\ &\to \frac{1}{S_{\rm lin}(E)}\frac{1}{\Gamma_{\rm cl} t} \end{aligned} \tag{66}$$

if initially only states with energy around E are populated. Three qualitatively different energy regimes can be distinguished [Fig. 11]. At the quantization energy $E = \phi$, $S_{\rm lin}(E)$ reaches its peak; the peak height scales as λ^{-1} for small λ, and its width scales as λ compared to the peak spacing. This is in fact the energy region which dominates the tail of the wavefunction intensity distribution in Section V. Away from the peak, for $|E-\phi| \gg \lambda$, the linearized LDOS falls off exponentially:

$$S_{\rm lin}(E) \approx \frac{2\pi}{\lambda} e^{-\pi|E-\phi|/2\lambda} . \tag{67}$$

[Notice that for simplicity the above expression and those to follow are given in quasienergy units, where the spacing between successive scarring peaks is fixed at 2π. A factor of $T_P/\hbar$, where T_P is the orbit period in real time units, needs to be inserted to convert E to a real energy.]

Within $O(\lambda)$ of the antiscarring energy $E = \phi + \pi$ (this is the energy equidistant between two successive scarring peaks), the LDOS rolls over smoothly to attain the minimum value

$$S_{\rm lin}(E = \phi + \pi) \approx \frac{4\pi}{\lambda} e^{-\pi^2/2\lambda} . \tag{68}$$

The region within $O(\lambda)$ of the antiscarring energy $E = \phi + \pi$ is thus responsible for producing the smallest wavefunction intensities, and the narrowest resonances in the corresponding open system. This excess of exponentially small decay rates is as dramatic a signature of the underlying classical behavior as the long wavefunction intensity tails found in Section V.

Energy-averaging allows us to sample resonances from all three energy regimes: wide resonances from near $E = \phi$, very narrow resonances from near $E = \phi + \pi$, and intermediate-width resonances from the region described by Eq. 67 (the same can be accomplished by varying a weak magnetic field at constant energy and thus sweeping through different values of the phase ϕ). The total probability to remain in the system at short times is given by

$$P_{\rm rem} = 1 - < S_{\rm lin} > \Gamma t/N = 1 - \Gamma_{\rm cl} t \tag{69}$$

(where we use the first line of Eq. 66 and notice that $< S_{\rm lin} >= A_{\rm lin}(0) = \langle a|a\rangle = 1$ by normalization). Thus at short times $t \ll \Gamma_{\rm cl}^{-1}$, the faster-decaying scarred states and slower-decaying antiscarred states always cancel exactly to produce a result consistent with our classical expectations. At long times, we use the second line of Eq. 66 to obtain

$$P_{\rm rem}(t) = \frac{< S_{\rm lin}^{-1} >}{\Gamma_{\rm cl} t} . \tag{70}$$

In the strong scarring regime of small λ, the average $< S_{\rm lin}^{-1} >$ is dominated by narrow resonances within $O(\lambda)$ of the antiscarring energy $E = \phi$ (Eq. 68), and gives an exponentially large (in λ) enhancement over the predictions of RMT:

$$< S_{\rm lin}^{-1} >= \left(\frac{\lambda}{2\pi}\right)^2 e^{\pi^2/2\lambda} . \tag{71}$$

Thus, the quantum mechanical probability to remain in the system at long times is very strongly dependent on the location of the opening relative to the unstable classical orbits of the system. This is in contrast with the classical long-time probability to remain, which for a small opening is independent of the location of the opening [the classical distribution continually being uniformly redistributed over the entire phase space, on a time scale very short compared to the decay time of the system]. See Figs. 12,13 later in this section for a numerical example.

Enhancements in the probability to remain at long times are obtained also for leads centered slightly away from the periodic orbit; in particular an enhancement of order $\lambda^2 e^{\pi^2/2\lambda}$ is found as long as the lead is within a phase space area scaling as $\lambda^2\hbar$ surrounding the orbit. Thus, the long-time probability to remain in the system averaged over all possible positions of the lead is given by

$$P_{\rm rem} = \frac{1 + O(\hbar\lambda^4 e^{\pi^2/2\lambda})}{\Gamma_{\rm cl} t} . \tag{72}$$

[In principle, contributions from all the periodic orbits need to be added, however, if orbits with small λ exist, they will clearly dominate any such sum.] The result is that at finite energy, exponentially large (in $1/\lambda$) deviations from RMT are found even after averaging over the lead position. In the $\hbar \to 0$ limit of any given classical system, the RMT behavior is recovered as the probability of the lead being within $\hbar$ of a short periodic orbit goes to zero.

Classically, not only is the long-time probability to remain independent of the lead position, but it is also largely independent of the initial probability distribution in the system (as long as this distribution is not concentrated in a very narrow corridor starting at the lead and having width scaling as the lead size). Similarly, the remaining classical probability distribution at long times is always evenly distributed in the classical phase space, again with the exception of a similar narrow corridor. Both of these statements are modified by quantum mechanical effects associated with the unstable periodic orbits of the system [14]. In the non-overlapping resonance regime of small Γ, the long-time probability to remain in state $|b\rangle$ given a decay channel at $|a\rangle$, as well as the total probability to remain in the system given an initial probability concentrated at $|a\rangle$ are *both* given by

$$P_{\rm rem}^b(t) = \sum_n |\langle b|n\rangle|^2 e^{-\Gamma_n t} . \tag{73}$$

If $|b\rangle$ is not located on the same short periodic orbit as $|a\rangle$ (and not related to it by symmetry), the intensities $|\langle b|n\rangle|^2$ follow a chi-squared distribution independent of the decay rates $\Gamma_n \sim |\langle a|n\rangle|^2$, and the mean value of this

intensity at a given energy scales as $S^b_{\rm lin}$, the smoothed LDOS at $|b\rangle$. Then at energy E we have

$$P^b_{\rm rem} = \frac{S^b_{\rm lin}(E)}{1 + S^a_{\rm lin}(E)\Gamma t/N} \to \frac{S^b_{\rm lin}(E)}{S^a_{\rm lin}(E)} \frac{1}{\Gamma_{\rm cl} t} \,. \qquad (74)$$

Again averaging over energy we obtain the long-time ratio of the remaining probability density at $|b\rangle$ compared to the average remaining probability density at long times:

$$\frac{P^b_{\rm rem}}{P_{\rm rem}} = \frac{< S^b_{\rm lin}/S^a_{\rm lin} >}{< 1/S^a_{\rm lin} >} \,. \qquad (75)$$

The ratio obtained above strongly deviates from unity if both $|a\rangle$ and $|b\rangle$ are located on short unstable periodic orbits, so that their linearized spectral envelopes $S^b_{\rm lin}$ and $S^a_{\rm lin}$ are nontrivial. Consider two specific cases. If $S^a_{\rm lin}$ and $S^b_{\rm lin}$ are located on (distinct) periodic orbits of the same classical period, action, and stability exponent λ, then the two envelopes are identical and we obtain the exponential suppression

$$\frac{P^b_{\rm rem}}{P_{\rm rem}} =< (S^a_{\rm lin})^{-1} >^{-1} \sim \lambda^{-2} e^{-\pi^2/2\lambda} \,. \qquad (76)$$

On the other hand, if the two spectral envelopes are exactly out of phase in the region of interest, i.e. $S^b_{\rm lin}(E) = S^a_{\rm lin}(E + \pi)$, the ratio is dominated by the peak in $S^b_{\rm lin}$, and becomes an *enhancement* factor λ^{-1} for small λ. We note that this suppression or enhancement of probability on orbits *other* than the one on which the lead is located is of course a quantum interference effect, having no counterpart in the classical dynamics of the system. Even stronger interference effects are observed on the orbit where the lead is located, due to the very strong correlations (found in Section VI) between densities of states at different points on the same orbit; see [14] for details.

The data in this section is taken from [14], and was originally obtained using an ensemble of perturbed cat maps. See [14] for a fuller discussion of the numerical evidence. In Fig. 12 is shown the measured probability to remain in the system as a function of scaled time $t' = \Gamma_{\rm cl} t$, for a generic lead location (plusses) and for a lead placed on an unstable periodic orbit with exponent $\lambda = 0.96$ (squares). The classical exponential decay law (dotted curve) is shown for comparison. We see that the numerical results for a generically placed lead agree well with the RMT prediction of Eq. 62, shown as a dashed line. The long-time probability to remain given a lead placed on the periodic orbit shows a large enhancement factor, consistent with the theoretical prediction of Eq. 70 (solid line). For this value of λ, the predicted enhancement factor at long times is 11.0. The numerical data is obtained for a system size $N = 120$, and the decay rate per step in the exit channel is $\Gamma = 0.1$.

In Fig. 13, the predicted enhancement factor $< S^{-1}_{\rm lin} >$ in the long-time probability to remain is plotted as a solid curve, as a function of the instability exponent λ of the orbit on which the lead is located. The prediction is valid in the semiclassical limit $N \to \infty$; numerical data is presented for $N = 120$ (plusses) and $N = 240$ (squares). We notice the very large enhancement factors that are obtained even for moderate values of λ, in accordance with the exponential asymptotic behavior of Eq. 71. Finally, in Fig. 14 we give an example of the enhancement and suppression of intensity at long times found on an orbit other than the one on which the lead is located, as the relative phase between the two orbits is varied. In practice, a curve of this kind can be obtained by varying a magnetic flux line or a weak magnetic field enclosed by one of the orbits. The theoretical prediction (Eq. 75) and numerical data are obtained for the case where both orbits have instability $\lambda = 1.76$. Because the stretching factor e^λ for one iteration of the orbit is quite large, both the intensity suppression when the orbits are in phase, and the enhancement when the two orbits are out of phase are quite moderate in this example.

An application of scarring methods to the study of conductance peaks in chaotic system with two leads is upcoming [15]; here we summarize the ideas and the major results. We again consider the regime where the leads are narrow (and the temperature low), so that the resonance peak width is small compared to the level spacing. The height of the n-th conductance peak is then given in the appropriate units by

$$G \sim \frac{\Gamma_{na}\Gamma_{nb}}{\Gamma_{na} + \Gamma_{nb}} \,, \qquad (77)$$

where Γ_{na}, Γ_{nb} are the decay rates of the n-th resonance through each of the two leads. If the openings are of the same size, this reduces to

$$G \sim \frac{|\langle n|a\rangle|^2 |\langle n|b\rangle|^2}{|\langle n|a\rangle|^2 + |\langle n|b\rangle|^2} \,, \qquad (78)$$

where we have taken out an overall constant proportional to the size of the opening. In RMT, the two intensities $|\langle n|a\rangle|^2$ and $|\langle n|b\rangle|^2$ are of course taken to be independent chi-squared variables (of one or two degrees of freedom, for real or complex overlaps, respectively), producing the desired distribution of peak heights. Several situations are now considered which show marked deviations from the RMT predictions.

(i) One of the leads, say a, is optimally placed on a short unstable periodic orbit, of exponent λ. Then conductance peak heights show periodic fluctuations in energy, with larger conductances at the scarring energies, and smaller conductances far from these energies. In particular, for small λ the mean value of $|\langle n|a\rangle|^2$ becomes large (as λ^{-1}) at the peak scarring energies, and the peak heights are then governed entirely by the fluctuations in $|\langle n|b\rangle|^2$. Near the minimum of $S^a_{\rm lin}$, the effect is more dramatic: the peak height again becomes a simple chi-squared variable, here governed entirely by fluctuations in $|\langle n|a\rangle|^2$, but the mean value of the peak height is exponentially small in λ (see Eq. 68). A fraction of $O(\lambda)$ of all

peaks will have the suppression of Eq. 68; this excess of exponentially small conductance peaks will of course persist after averaging over either energy or weak magnetic field strength.

(ii) The two leads are placed on two orbits whose spectral envelopes are "in phase" in the energy range of interest. Say for simplicity that the two orbits also have the same exponent λ, so $S^a_{\rm lin} = S^b_{\rm lin}$. At each energy, the conductance peak heights now follow the same distribution as in RMT, but the mean value is proportional to $S_{\rm lin}(E)$. Thus, at the scarring energies the conductance peak heights are increased by $O(\lambda^{-1})$ over the mean RMT value, whereas at the antiscarring energies the heights are suppressed by $O(\lambda^2 e^{-\pi^2/2\lambda})$. The energy-averaged (or magnetic-field averaged) distribution can also be obtained, and shows an enhancement in probability for large and small peak heights (compare the tail of the wavefunction intensity distribution in Section V).

(iii) The two orbits are "out of phase". Then strong suppression of conductance peak heights is predicted everywhere, and the mean peak height is also exponentially small in λ. The largest peak heights appear at energies intermediate between the maxima of $S^a_{\rm lin}$ and $S^b_{\rm lin}$, where $S^a_{\rm lin} \approx S^b_{\rm lin}$. Even at these energies, the conductance is exponentially suppressed compared to the RMT prediction.

(iv) The two leads are located on the same orbit, or on two orbits related by a symmetry. Here $|\langle n|a\rangle|^2 = |\langle n|b\rangle|^2$, and the peak height distribution is again given by a simple chi-squared distribution, with mean given by $S_{\rm lin}(E)$. The energy-averaged mean peak height is independent of the stability exponent λ, but once again we predict power-law (in λ) enhancement of the conductance near the scarring energies, and exponential suppression near the antiscarring energies.

VIII. CONCLUSION

We have seen that short unstable periodic orbits leave a strong imprint on the long-time and stationary properties of a quantum chaotic system, even though the corresponding classical dynamics loses all memory of these structures at long times. This insight can be extended to other situations where short-time classical structures lead to modifications of RMT predictions concerning the structure of quantum wavefunctions. Sundaram and Scharf [44] study periodic orbits in *complex* phase space, with complex action, and show that these "ghost" orbits can also produce wavefunction scars.

All of the discussion in the present paper applies to isolated orbits in a system of any dimension, though specific formulas need to be adjusted to take proper account of multi-dimensional Gaussian wavepackets and their short-time evolution. In higher-dimensional chaotic systems, classically invariant manifolds containing large families of individual orbits can also lead to scar-like effects, if the classical rate of escape away from these manifolds is slow. Examples include highly excited eigenstates in three-dimensional billiards [45] and wavefunctions of few-body chaotic systems made up of identical particles with rotation and permutation symmetries [46].

Vilela Mendes has analyzed "saddle scars," structures which arise from unstable harmonic motion along the stable manifold of a classical saddle point [47]. Blumel et al. extend quantum chaos techniques, including analysis of scars, to problems in which ray splitting surfaces are present [48]. Delande and Sornette study acoustic radiation from membranes, and find localization in the radiation directivity that can be attributed to wavefunction scars [49]

The insights of scar theory can be extended also to short-time effects not associated with any classical structures. These short-time recurrences may result from diffractive scattering or other hard quantum dynamics far from the semiclassical regime. Thus, in a diffusive system, the local, short-time behavior of a quantum particle may lead in certain models to strong effects on the statistics of anomalous wavefunctions, effects not captured by the standard field theory methods [41] which generally ignore dynamics on scales shorter than a mean free path. The scar picture may prove to be a unifying framework for studying anomalous localization on graphs, lattices, in disordered systems, and in S-matrix eigenstates. These extensions of scar ideas to non-classical short-time behavior are now under development.

IX. ACKNOWLEDGEMENTS

This research was supported by the National Science Foundation under Grant No. 66-701-7557-2-30.

[1] S. W. McDonald, Lawrence Berkeley Lab. Report LBL-14837 (1983).
[2] E. J. Heller, *Phys. Rev. Lett.* **53**, 1515 (1984).
[3] M. V. Berry, in *Chaotic Behaviour of Deterministic Systems*, ed. by G. Iooss, R. Helleman, and R. Stora (North-Holland 1983) p. 171.
[4] M. V. Berry and M. Tabor, *Proc. Roy. Soc.* **A 349**, 101 (1976); M. V. Berry and M. Tabor, *J. Phys.* **A 10**, 371 (1977).
[5] A. I. Schnirelman, *Usp. Mat. Nauk.* **29**, 181 (1974); Y. Colin de Verdiere, *Commun. Math. Phys.* **102**, 497 (1985); S. Zelditch, *Duke Math. J.* **55**, 919 (1987).
[6] L. Kaplan and E. J. Heller, Weak Quantum Ergodicity, *Physica* **D**, in press.
[7] O. Bohigas, M.-J. Giannoni, and C. Schmit, *J. Physique Lett.* **45**, L-1015 (1984).
[8] M. C. Gutzwiller, *J. Math. Phys.* **8**, 1979 (1967); *J. Math. Phys.* **10**, 1004 (1969); *J. Math. Phys.* **12**, 343 (1971).

[9] P. O'Connor, J. N. Gehlen, and E. J. Heller, *Phys. Rev. Lett.* **58**, 1296 (1987).
[10] S. Tomsovic and E. J. Heller, *Phys. Rev. Lett.* **70**, 1405 (1993); S. Tomsovic and E. J. Heller, *Phys. Rev.* **E 47**, 2821 (1993); L. Kaplan, Multiplicative semiclassical dynamics and the quantization time, *Phys. Rev.* **E**, in press.
[11] L. Kaplan and E. J. Heller, *Ann. Phys. (N. Y.)* **264**, 171 (1998).
[12] L. Kaplan, *Phys. Rev. Lett.* **80**, 2582 (1998).
[13] L. Kaplan and E. J. Heller, *Universal scarmometers: scarring beyond the Gaussian wavepacket* (preprint, 1998).
[14] L. Kaplan, *Scar and antiscar quantum effects in open chaotic systems* (preprint, 1998).
[15] W. E. Bies, L. Kaplan, and E. J. Heller, *Quantum conductance peaks and periodic orbits in classically chaotic systems* (preprint, 1998).
[16] S. Sridhar, *Phys. Rev. Lett* **67**, 785 (1991); S. Srdihar, D. O. Hogenboom, and B. A. Willemsen, *J. Stat. Phys.* **68**, 239 (1992).
[17] J. Stein and H.-J. Stöckman, *Phys. Rev. Lett.* **68**, 2867 (1992).
[18] T. M. Fromhold, P. B. Wilkinson, F. W. Sheard, L. Eaves, J. Miao, and G. Edwards, *Phys. Rev. Lett.* **75**, 1142 (1995); P. B. Wilkinson, T. M. Fromhold, L. Eaves, F. W. Sheard, N. Miura, and T. Takamasu, *Nature* **380**, 608 (1996).
[19] E. E. Narimanov and A. D. Stone, *Phys. Rev. Lett.* **80**, 49 (1998).
[20] D. Wintgen and A. Honig, *Phys. Rev. Lett.* **63**, 1467 (1989); K. Muller and D. Wintgen, *J. Phys.* **B 27**, 2693 (1994).
[21] B. Li, *Phys. Rev.* **E 55**, 5376 (1997); B. Li and B. Hu, *J. Phys.* **A 31**, 483 (1998).
[22] W. E. Bies, L. Kaplan, and E. J. Heller, *On scarring in the stadium billiard* (preprint, 1998).
[23] A. Bäcker, R. Schubert, and P. Stifter, *Phys. Rev.* **E 57**, 5425 (1998).
[24] F. P. Simonotti, E. Vergini, and M. Saraceno, *Phys. Rev.* **E 56**, 3859 (1997).
[25] T. M. Antonsen, Jr., E. Ott, Q. Chen, and R. N. Oerter, *Phys. Rev.* **E 51**, 111 (1995).
[26] E. B. Bogomolny, *Physica* **D 31**, 169 (1988).
[27] M. V. Berry, Les Houches Lecture Notes, Summer School on Chaos and Quantum Physics, M-J. Giannoni, A. Voros, and J. Zinn-Justin, eds., Elsevier Science Publishers B.V. (1991); M.V. Berry, *Proc. Roy. Soc.* **A 243**, 219 (1989).
[28] M. A. Sepulveda, S. Tomsovic, and E. J. Heller, *Phys. Rev. Lett.* **69**, 402 (1992).
[29] O. Agam and S. Fishman, *Phys. Rev. Lett.* **73**, 806 (1994); O. Agam and S. Fishman, *J. Phys.* **A 26**, 2113 (1993); O. Agam and N. Brenner, *J. Phys.* **A 28**, 1345 (1995); S. Fishman, B. Georgeot, and R. E. Prange, *J. Phys.* **A 29**, 919 (1996).
[30] G. G. de Polavieja, F. Borondo, and R. M. Benito, *Phys. Rev. Lett.* **73**, 1613 (1994).
[31] D. Klakow and U. Smilansky, *J. Phys.* **A 29**, 3213 (1996).
[32] A. M. O. de Almeida, *Phys. Rep.* **295**, 265 (1998).
[33] S. Tomsovic, *Phys. Rev. Lett.* **77**,4158 (1996).
[34] F. J. Arranz, F. Borondo, and R. M. Benito, *Phys. Rev. Lett.* **80**, 944 (1998).
[35] S. Nonnenmacher and A. Voros, *J. Phys.* **A 30**, 295 (1997).
[36] M. Saraceno, *Ann. Phys. (N. Y.)* **199**, 37 (1990).
[37] P. W. O'Connor and S. Tomsovic, *Ann. Phys. (N. Y.)* **207**, 218 (1991).
[38] E. J. Heller, *J. Chem. Phys.* **72**, 1337 (1980); E. J. Heller and M. J. Davis, *J. Phys. Chem.* **86**, 2118 (1982); E. B. Stechel and E. J. Heller, *Ann. Rev. Phys. Chem.* **35**, 563 (1984); E. J. Heller, *Phys. Rev.* **A35**, 1360 (1987).
[39] P. W. O'Connor, S. Tomsovic and E. J. Heller, *Physica* **D 55**, 340 (1992).
[40] L. Kaplan and E. J. Heller, *Phys. Rev. Lett.* **76**, 1453 (1996); F.-M. Dittes, E. Doron, and U. Smilansky, *Phys. Rev.* **E 49**, R963 (1994).
[41] V. I. Fal'ko and K. B. Efetov, *Phys. Rev.* **B 52**, 17413 (1995); I. E. Smolyarenko and B. L. Altshuler, *Phys. Rev.* **B 55**, 10451 (1997).
[42] A. Lupu-Sax, I. Smolyarenko, L. Kaplan, and E. J. Heller, *Wavefunction Intensity Statistics in a Disordered System of Point Scatterers* (preprint, 1998).
[43] D. L. Miller, cond-mat/9801245.
[44] B. Sundaram and R. Scharf, *Physica* **D 83**, 257 (1995).
[45] T. Prosen, *Phys. Lett.* **A 233**, 332 (1997).
[46] T. Papenbrock, T. H. Seligman, and H. A. Weidenmuller, *Phys. Rev. Lett.* **80**, 3057 (1998).
[47] R. Vilela Mendes, *Phys. Lett.* **A 233**, 265 (1997).
[48] R. Blumel, T. M. Antonsen, Jr., B. Georgeot, E. Ott, and R. E. Prange, *Phys. Rev.* **E 53**, 3284 (1996).
[49] D. Delande and D. Sornette, *J. Acoust. Soc. America* **101**, 1793 (1997).

FIG. 1. In (a), the full spectrum is plotted along with the linear envelope (dotted line), an intermediate envelope corresponding to $|T| < 30$ (solid line), and a semiclassical intermediate envelope (dashed line). In (b), a portion of the spectrum (solid) is compared to the spectrum obtained using semiclassical eigenstates (dashed). In (c), the quantum spectrum has been divided out by the linear envelope of (a) (after [11]).

FIG. 2. A plot of the actual value of the inverse participation ratio (IPR) for a wavepacket centered on a periodic orbit (squares), *versus* the value predicted by the linear theory. IPR's in the semiclassical approximation are plotted using the '+' symbol, and IPR's in a baker map with random matrix theory nonlinear behavior are plotted with triangles (after [11]).

FIG. 3. The two-point spectral correlation function of the scaled spectrum (diamonds) is compared to the correlation function of the raw spectrum (plusses), after ensemble and energy averaging (after [11]).

FIG. 4. Cumulative wavefunction intensity distribution (a) as measured by a test state centered on a periodic orbit with instability $\lambda = \log 2$, plotted as the upper thick curve with scarring theory prediction given by dashed curve, and (b) averaged over the entire phase space of size $200h$, plotted as lower thick curve with theory given by solid curve. The dotted line is the Porter-Thomas law (after [12]).

FIG. 5. Cumulative wavefunction intensity distribution after ensemble averaging over systems with classical orbits of different instability exponents. The scar theory tail is given by the solid line, and the dotted curve is the RMT prediction (after [12]).

FIG. 6. The correlation C_{ab} (Eq. 47) between local densities of states for two wavepackets $|a\rangle$ and $|b\rangle$, lying on the same periodic orbit of instability exponent λ, is plotted as a function of width parameter z. The upper and lower curves correspond to $\lambda = \log 5$ and $\lambda = \log 10$, respectively. The width (along the unstable manifold) of wavepacket $|b\rangle$ is $e^{\lambda(n+z)}$ times that of $|a\rangle$, where n is an integer (after [13]).

FIG. 7. The inverse participation ratio (IPR) for hyperbolic test state $|\Psi\rangle$ is plotted versus the log-time cutoff T_0 (see Eqs. 50, 41), for various values of system size N. From bottom to top, the five curves correspond to $N = 50$, 100, 200, 400, and 800. For each N, 26 points are plotted, for $c = (1.1)^j$, $j = -20 \ldots + 5$. The orbit has exponent $\lambda = |\log 0.18|$. The upper dashed curve is the $N \to \infty$ theoretical prediction, which converges to the asymptotic prediction of Eq. 53 (lower dashed line) for large T_0. The linearized theory is expected to start breaking down for $c \geq 1$ (rightmost six points on each data curve) (after [13]).

FIG. 8. Smoothed local densities of states are plotted for the off-resonance universal hyperbolic test state $|\Psi\rangle$, for off-resonance angle θ ranging from 0 (tallest peak) in steps of $\pi/10$ (to the left), through -2π, on a periodic orbit with exponent $\lambda = |\log 0.18|$. The system size is $N = 800$, and the cut-off constant c is set to 0.6 (see Eq. 41) (after [13]).

FIG. 9. Husimi plots of the universal test state Ψ for off-resonance parameter values (a) $\theta/\lambda = 0.8$ and (b) $\theta/\lambda = 2.5$. The linearizable region is taken to be much larger than the displayed area of size $12\sqrt{\hbar} \times 12\sqrt{\hbar}$, centered on the periodic orbit (after [13]).

FIG. 10. Smoothed local densities of states for a Gaussian wavepacket placed on a period-2 orbit (double-peaked solid curve), and for the universal test state Ψ constructed on the same orbit (tall single peak). The dashed curves represent theoretical predictions based on the linearized dynamics near the periodic orbit in question. The periodic orbit has a total exponent $\lambda = |\log 0.168|$ over the two-step period (after [13]).

FIG. 11. Smoothed local densities of states $S_{\rm lin}(E)$ are plotted as a function of energy on a periodic orbit of instability exponent $\lambda = 0.20$ (solid curve) and on an orbit with $\lambda = 0.15$ (dashed curve). We observe the peak at the EBK quantization energy $E = 0$ which scales as λ^{-1}, the exponential decay between $E = 0$ and $E = \pi$ (Eq. 67), and the minimum at the anti-EBK energy $E = \pi$, which is exponentially small in λ (Eq. 68). The RMT prediction $S_{\rm lin}(E) = 1$, which is applicable away from any short periodic orbit, is plotted as a dotted line (after [14]).

FIG. 12. The probability to remain in the open quantum system is plotted as a function of scaled time $t' = \Gamma_{\rm cl} t$. The classical prediction $\exp(-t')$ is shown as a dotted curve. The quantum probability to remain for a generic lead location (plusses) compares well with the RMT prediction $1/(1+t')$ (dashed curve). For a lead placed on a short periodic orbit with instability exponent $\lambda = 0.96$, we obtain the enhanced long-time probability to remain (squares), which agrees with the scar theory prediction $< S_{\rm lin}^{-1} > /t'$ (solid line). The system size used for obtaining the data is $N = 120$ and the decay rate per step in the exit channel is $\Gamma = 0.1$ (after [14]).

FIG. 13. The long-time enhancement factor of the probability to remain in a system when the lead is placed on a periodic orbit is plotted as a function of the instability exponent of the orbit. Data is shown for $N = 120$ (plusses) and $N = 240$ (squares). The $N \to \infty$ theoretical prediction $< S_{\rm lin}^{-1} >$ is shown as a solid curve. We see the exponential increase in the probability to remain as the exponent λ decreases (the $\lambda \to 0$ asymptotic form is given in Eq. 71). For large λ, the enhancement factor converges to 1, the RMT prediction (after [14]).

FIG. 14. The predicted relative intensity at long times on a periodic orbit other than the one containing the lead is plotted as a function of the relative phase between the two orbits (solid curve). For reference, the phase-space averaged intensity is plotted as a dashed line. Intensity suppression is predicted and observed when the orbits are in phase, and enhancement is seen when the orbits are exactly out of phase. The data is collected for an ensemble of systems with $N = 80$, and each orbit has instability exponent $\lambda = 1.76$ (after [14]).

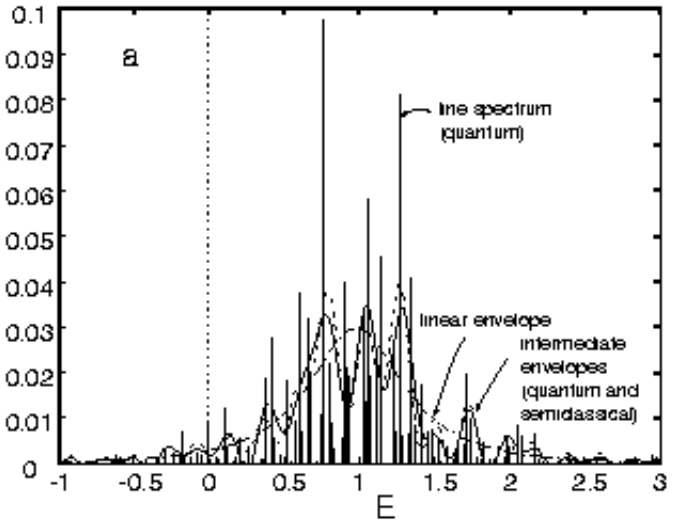
a
line spectrum
(quantum)
linear envelope
intermediate
envelopes
(quantum and
semidassical)
E

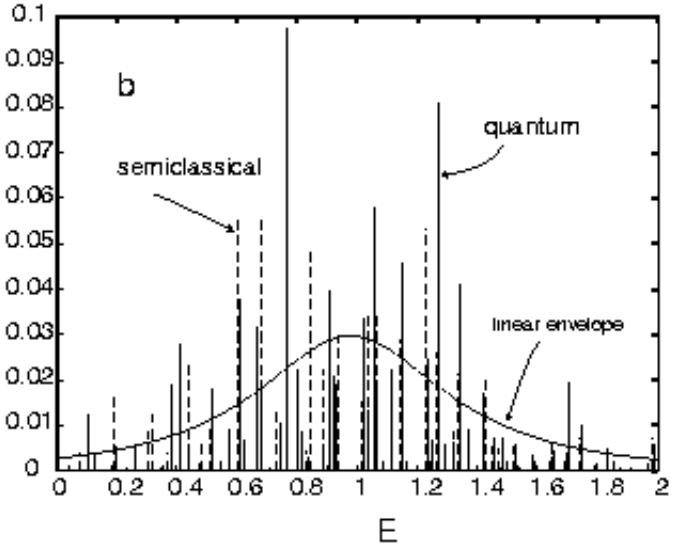
b
quantum
semiclassical
linear envelope
E

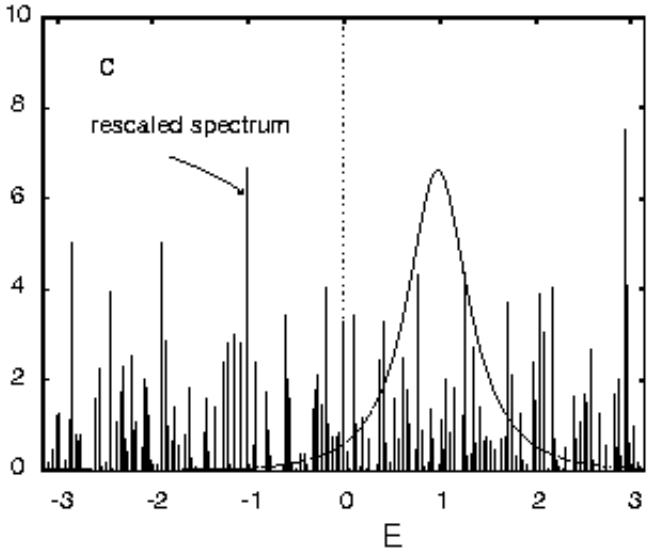
c
rescaled spectrum
E

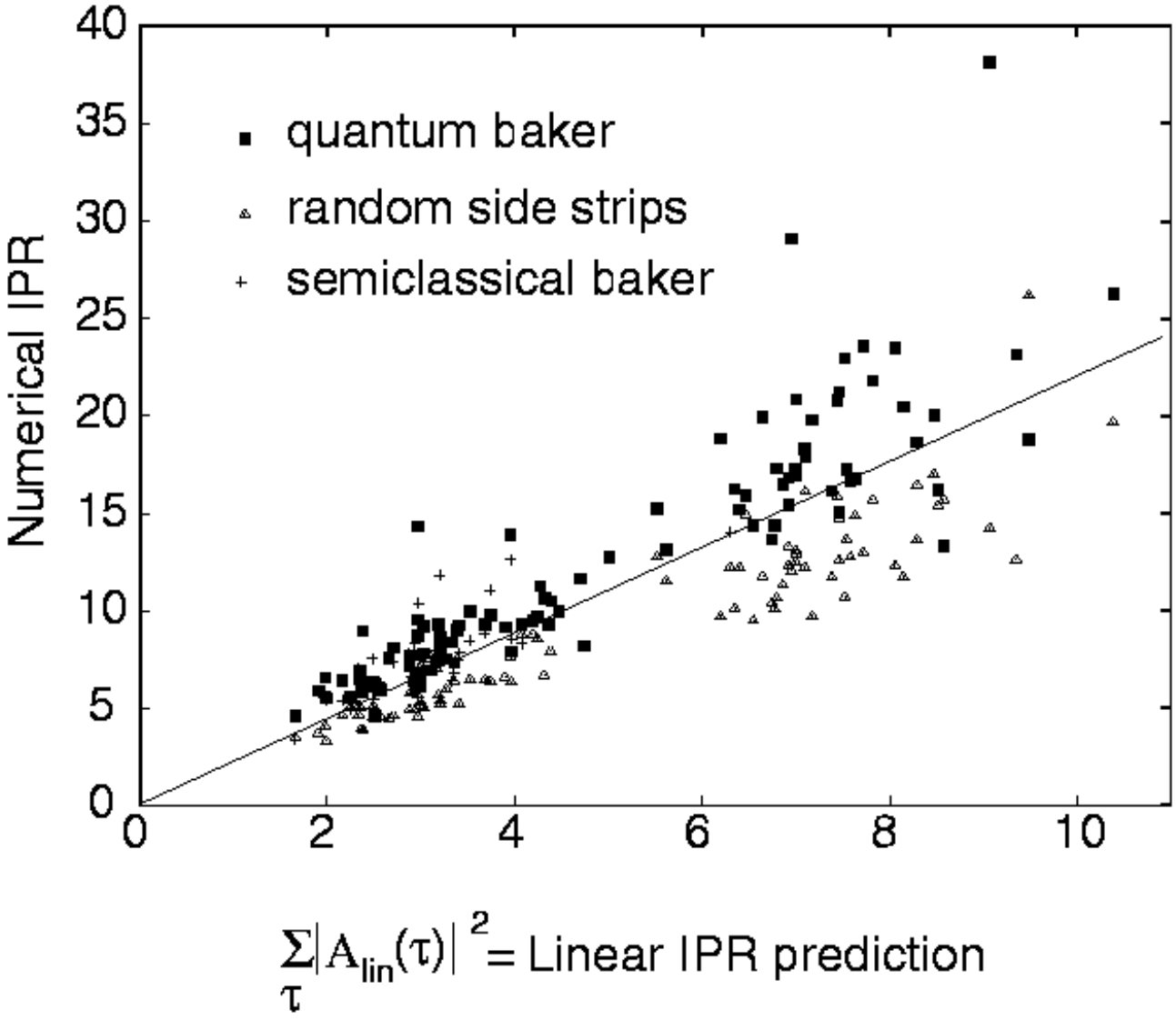
quantum baker
random side strips
semiclassical baker
Numerical IPR
0
5
10
15
20
25
30
35
40
0
2
4
6
8
10
$\sum_{\tau} |A_{lin}(\tau)|^2$ = Linear IPR prediction

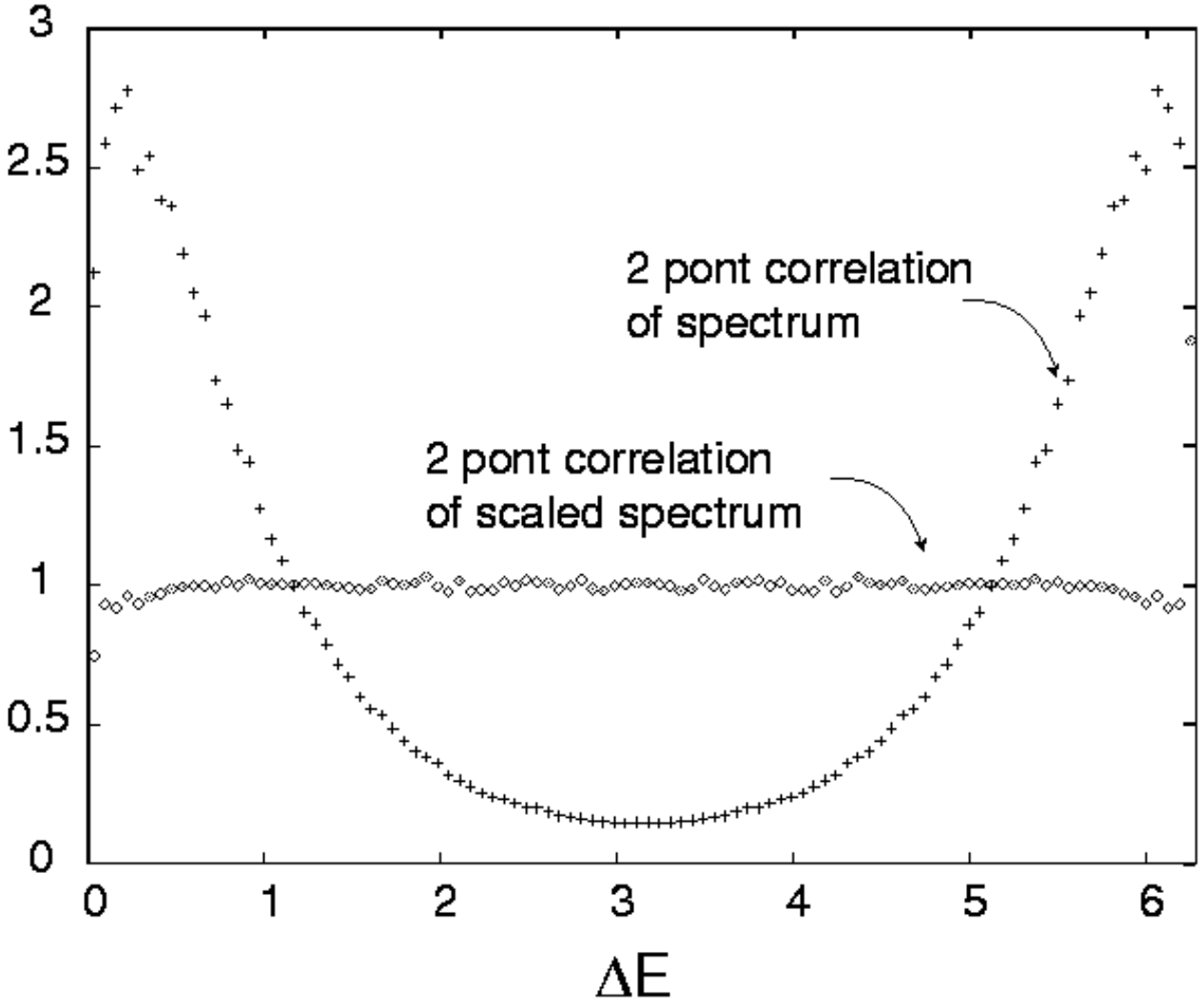
3
2.5
2
1.5
1
0.5
0
0
1
2
3
4
5
6
2 pont correlation
of spectrum
2 pont correlation
of scaled spectrum
ΔE

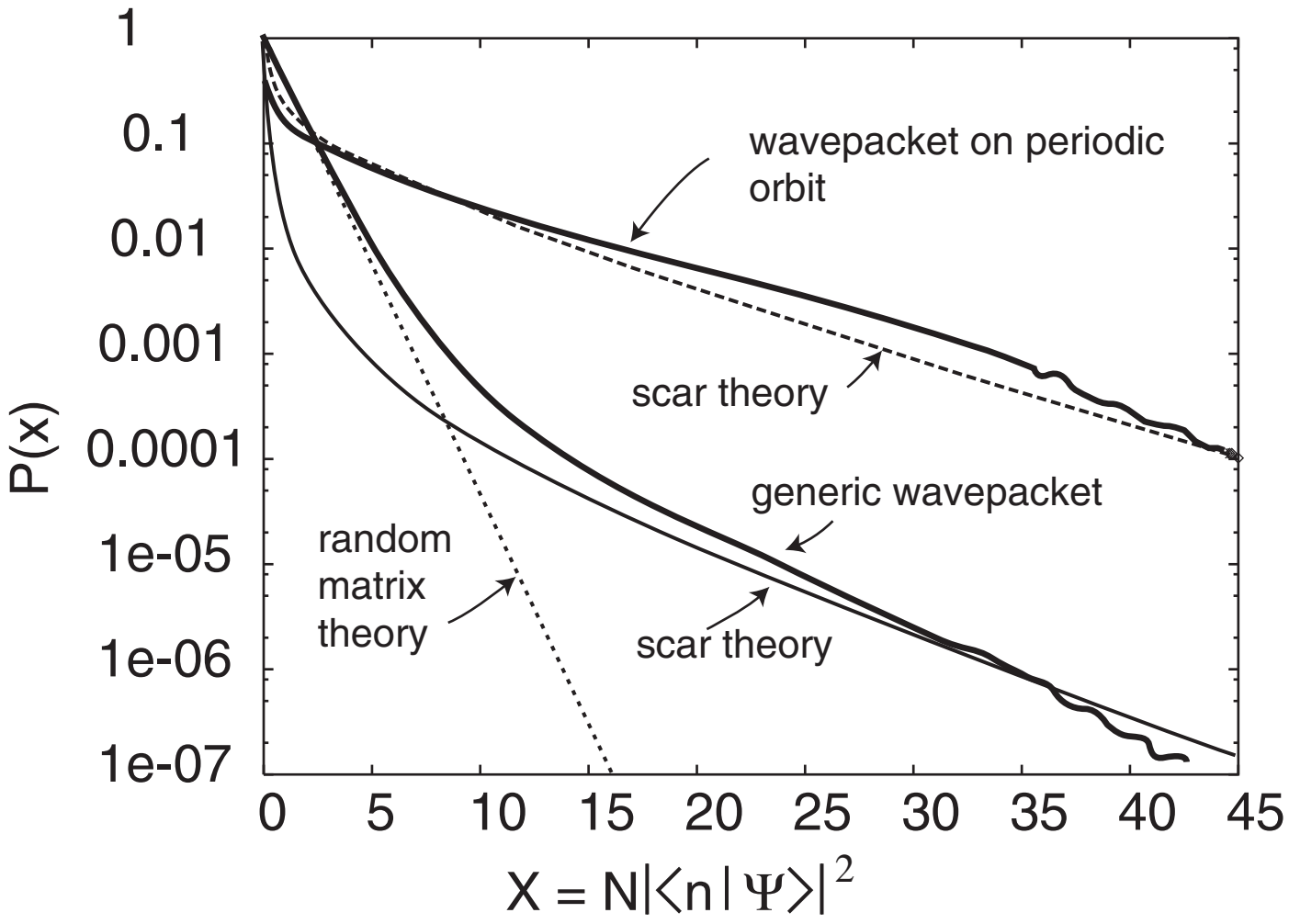
1
0.1
0.01
0.001
0.0001
1e-05
1e-06
1e-07
P(x)
0
5
10
15
20
25
30
35
40
45
X = N|<n|Ψ>|²
wavepacket on periodic orbit
scar theory
generic wavepacket
random matrix theory
scar theory

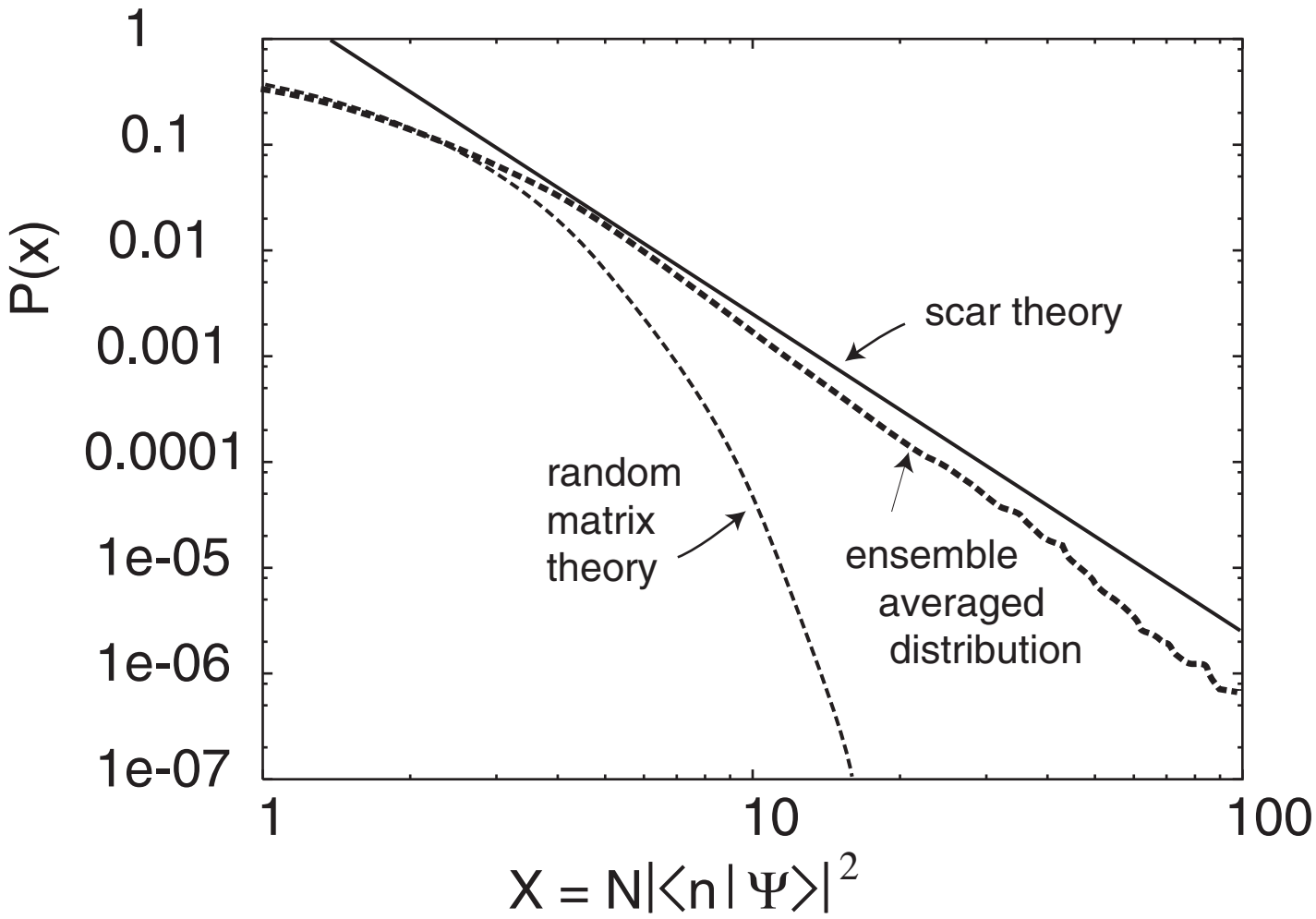
1
0.1
0.01
0.001
0.0001
1e-05
1e-06
1e-07
P(x)
1
10
100
X = N|<n|Ψ>|²
scar theory
random
matrix
theory
ensemble
averaged
distribution

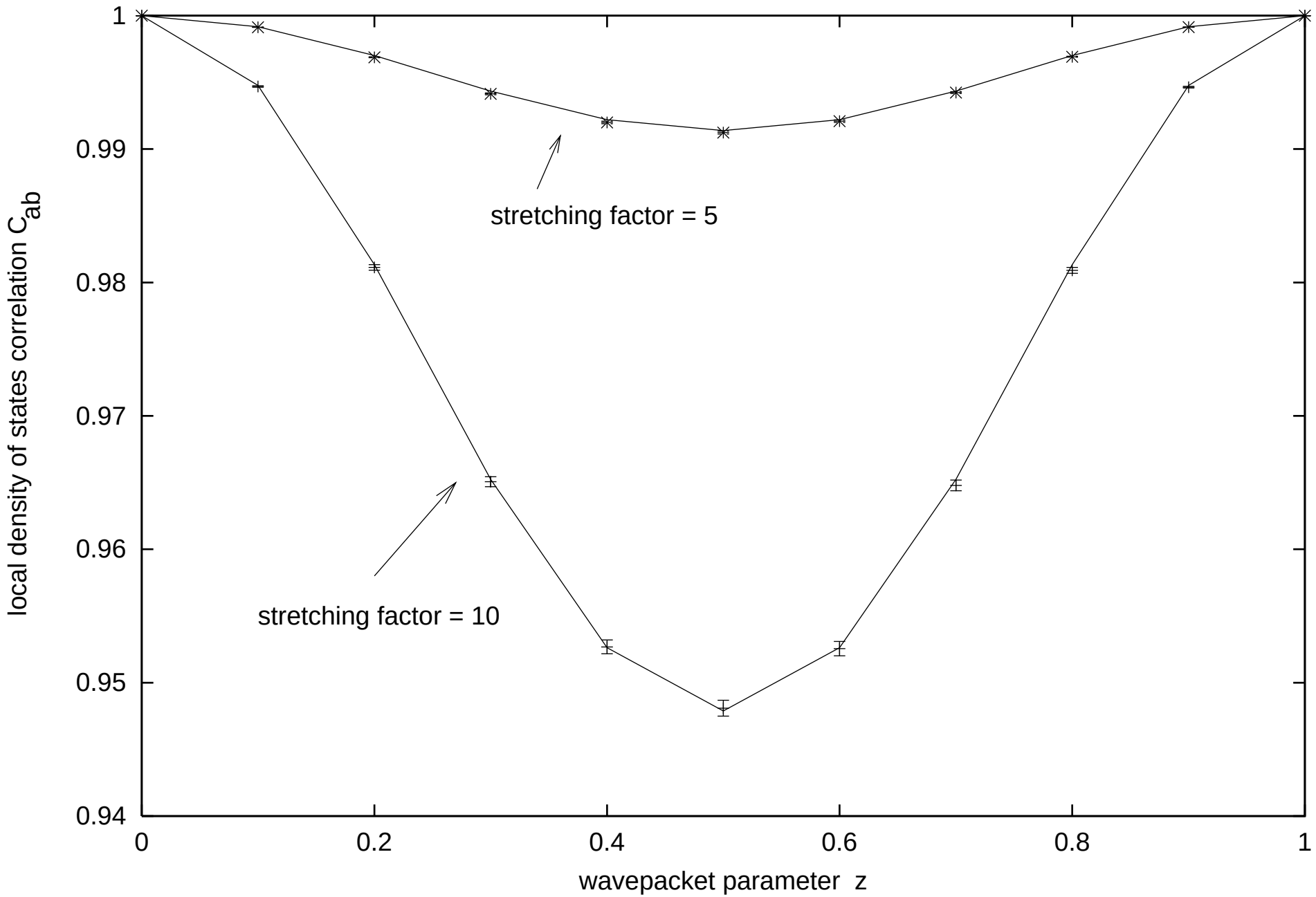
1
0.99
0.98
0.97
0.96
0.95
0.94
0
0.2
0.4
0.6
0.8
1
local density of states correlation C_{ab}
wavepacket parameter z
stretching factor = 5
stretching factor = 10

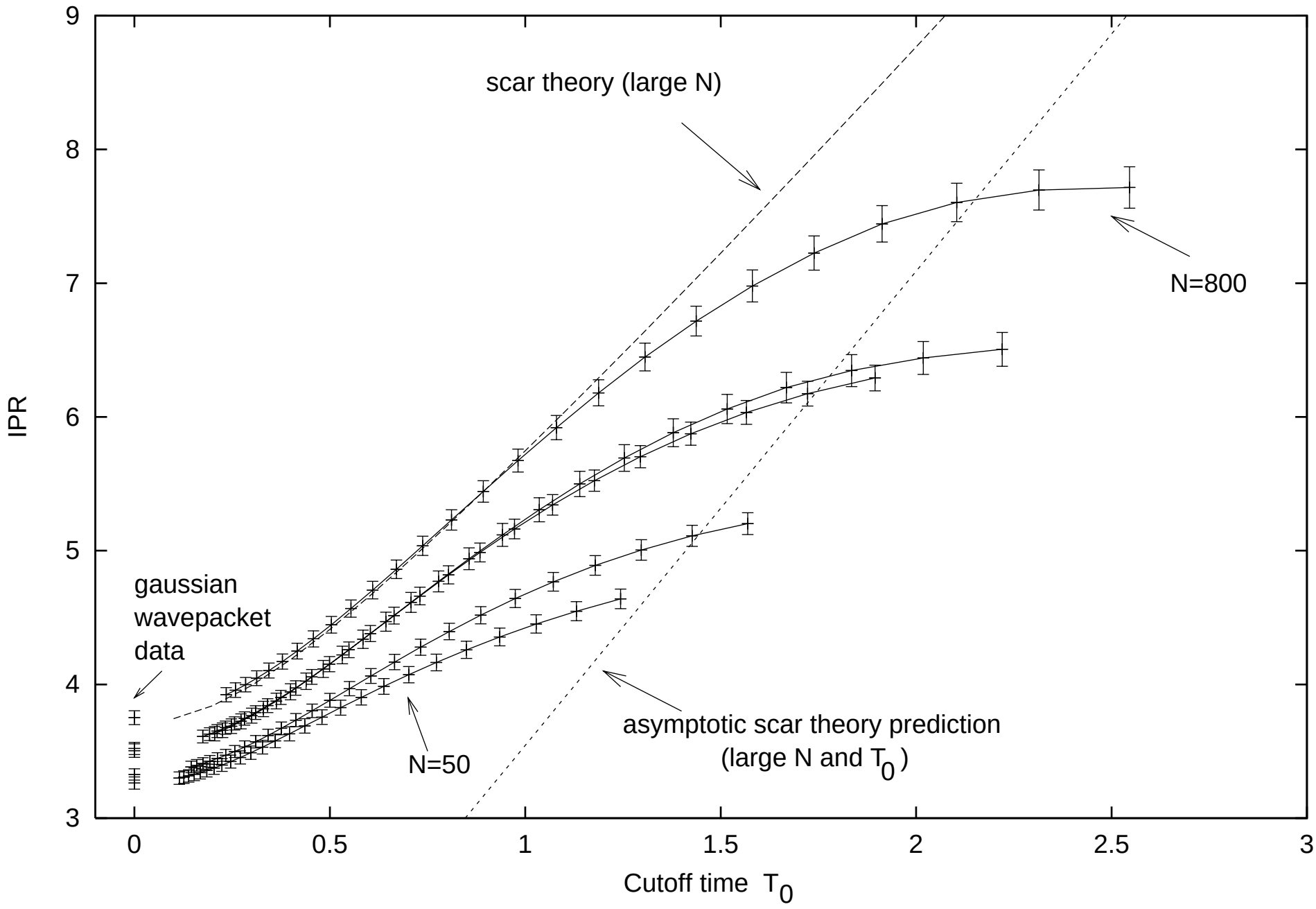
scar theory (large N)
N=800
N=50
gaussian
wavepacket
data
asymptotic scar theory prediction
(large N and T0)
IPR
Cutoff time T0
9
8
7
6
5
4
3
0
0.5
1
1.5
2
2.5
3

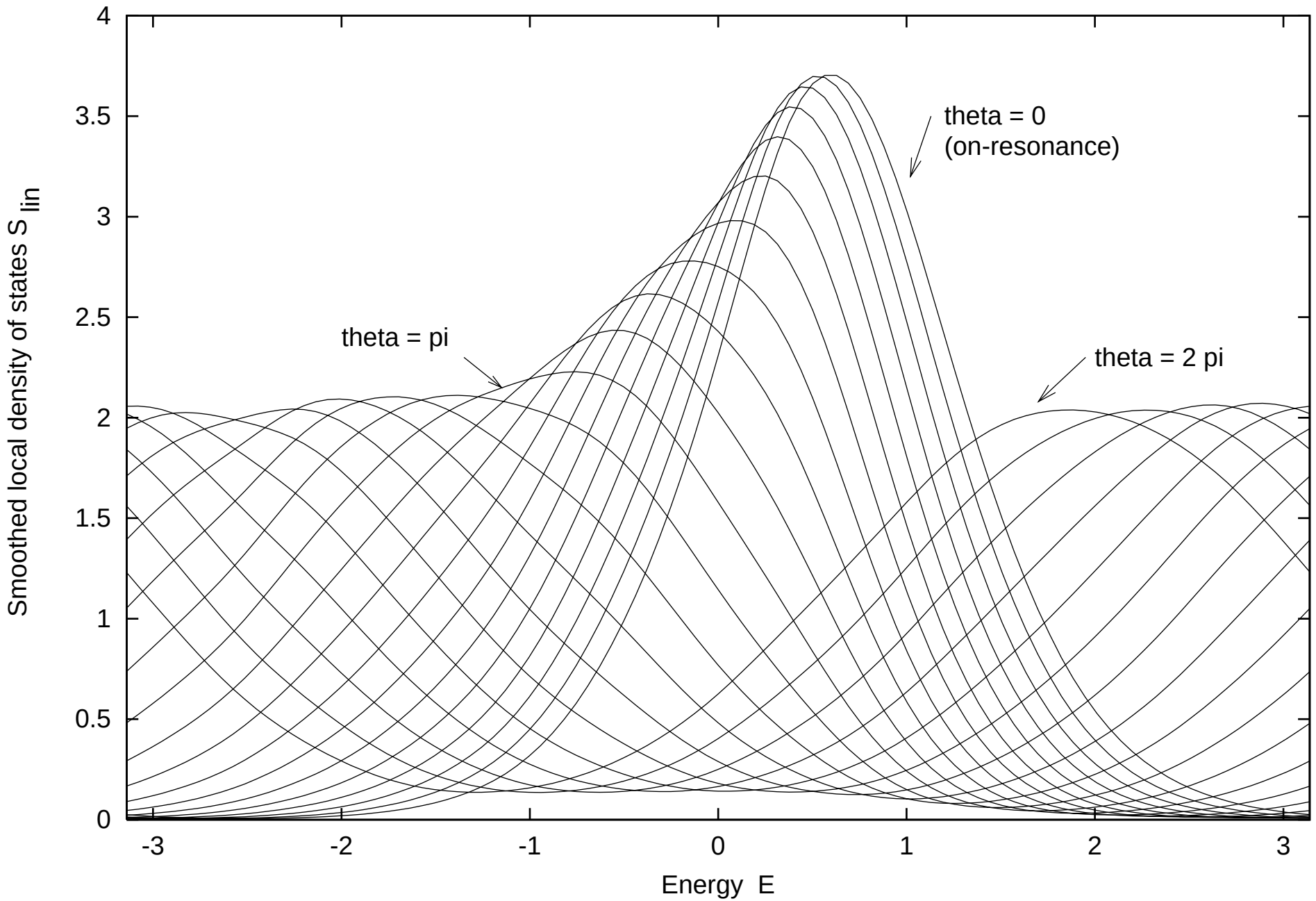
Smoothed local density of states S lin
Energy E
theta = 0
(on-resonance)
theta = pi
theta = 2 pi
4
3.5
3
2.5
2
1.5
1
0.5
0
-3
-2
-1
0
1
2
3

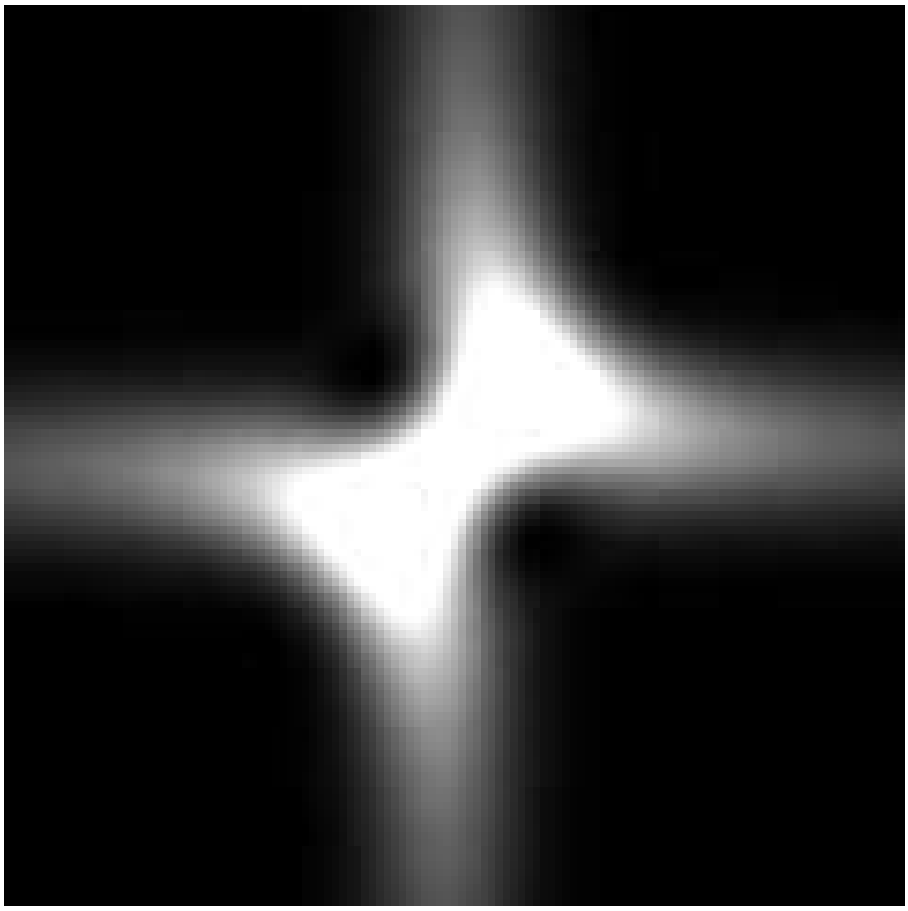

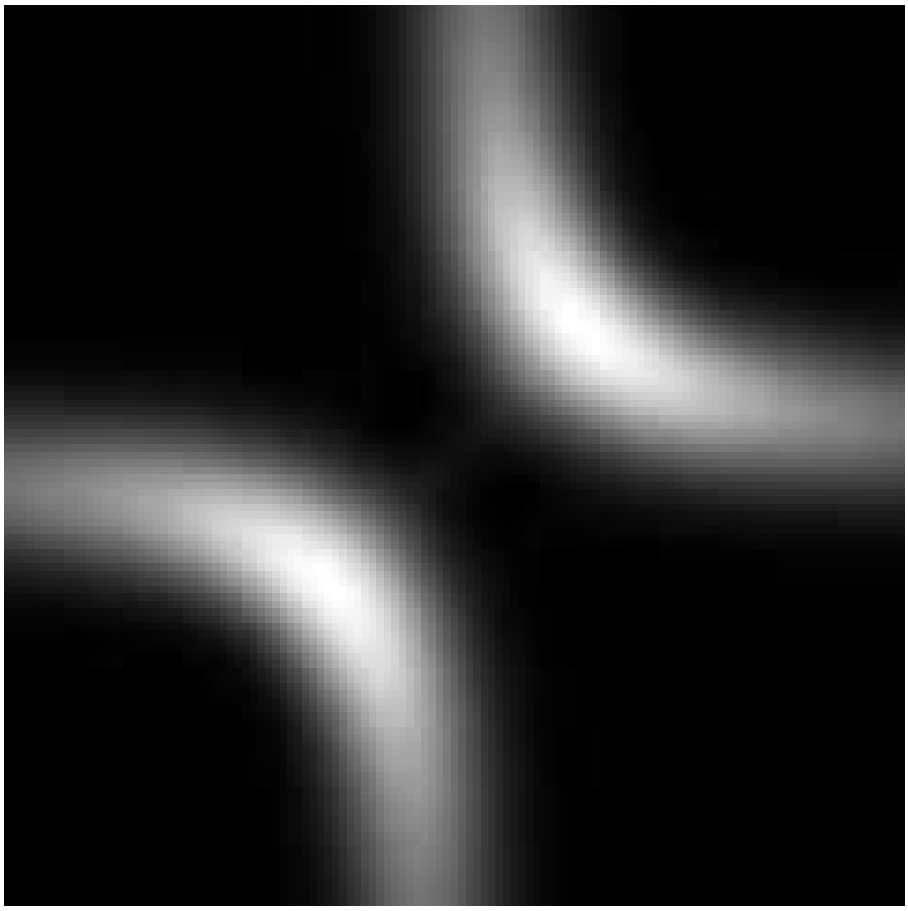

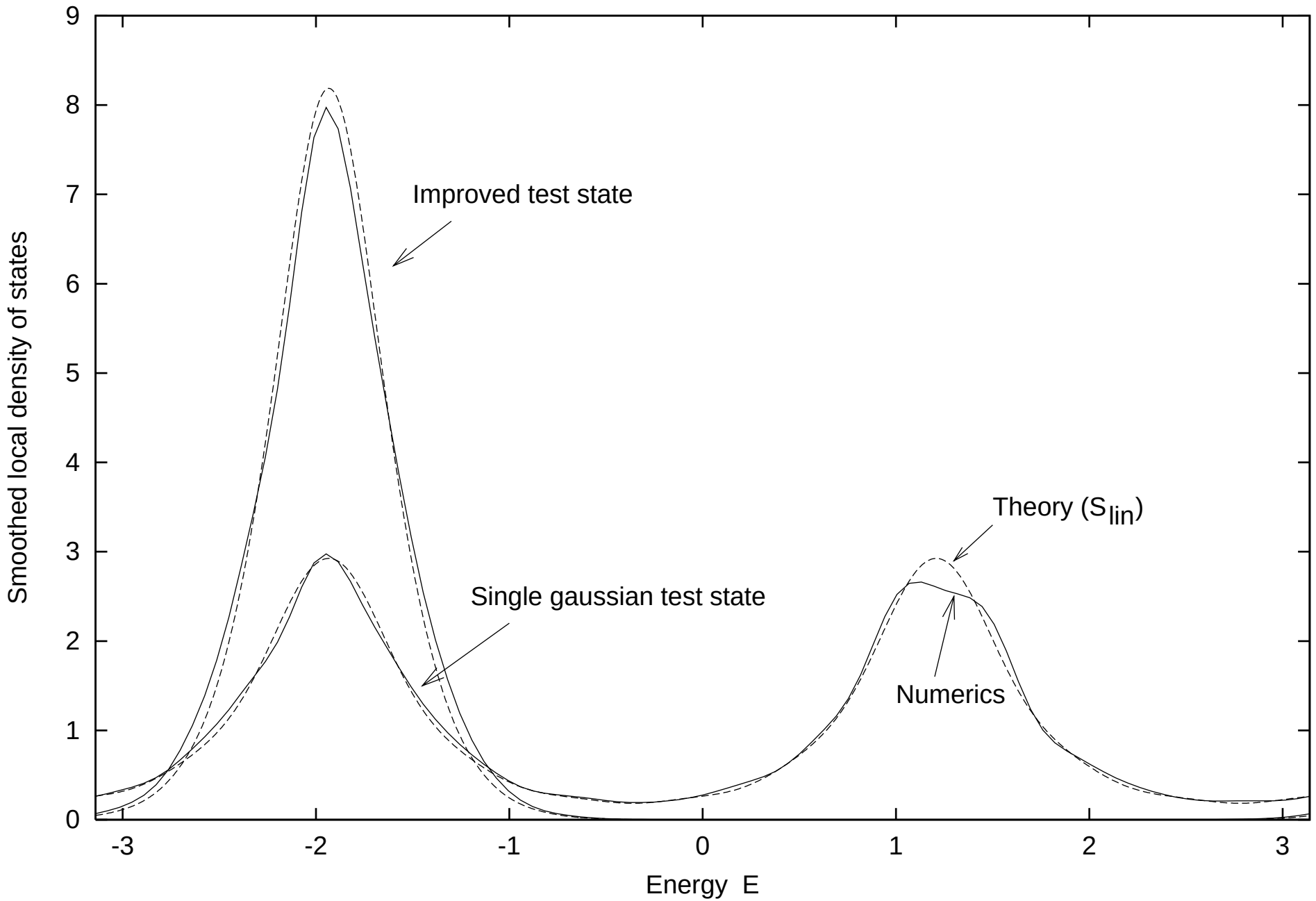
Smoothed local density of states
Energy E
Improved test state
Single gaussian test state
Theory (S_{lin})
Numerics
0
1
2
3
4
5
6
7
8
9
-3
-2
-1
0
1
2
3

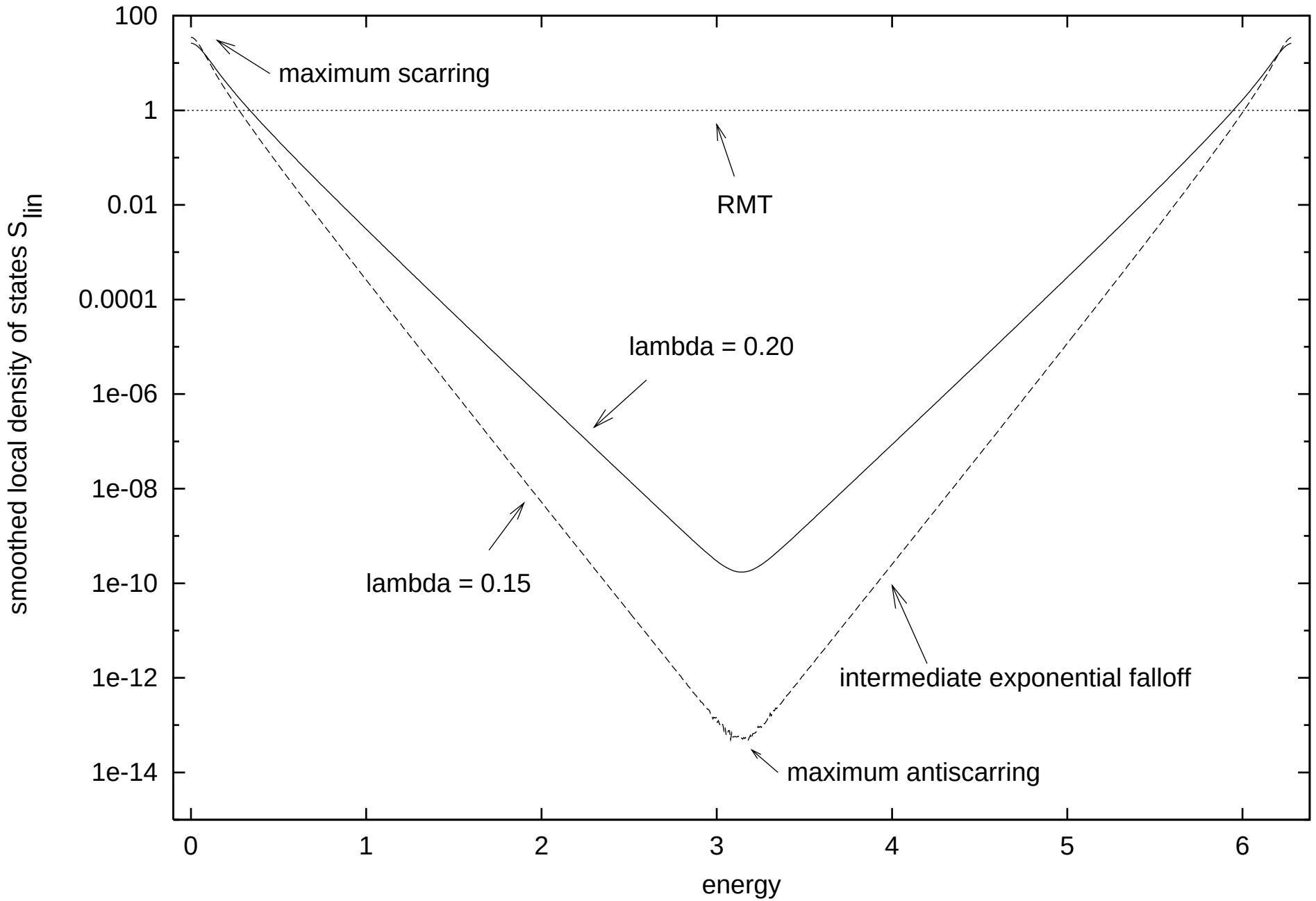
100
1
0.01
0.0001
1e-06
1e-08
1e-10
1e-12
1e-14
smoothed local density of states S_{lin}
0
1
2
3
4
5
6
energy
maximum scarring
RMT
lambda = 0.20
lambda = 0.15
intermediate exponential falloff
maximum antiscarring

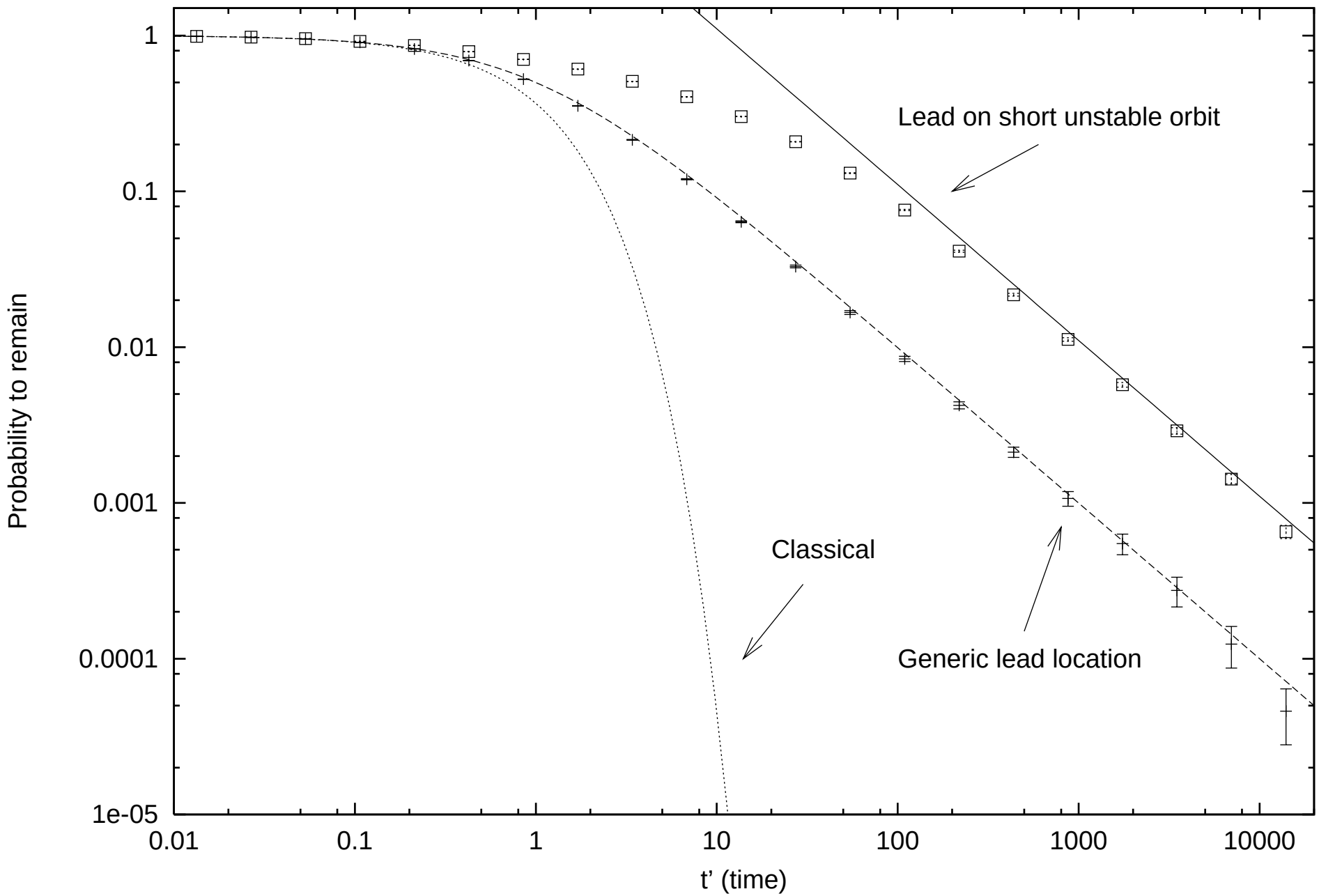
Probability to remain
1
0.1
0.01
0.001
0.0001
1e-05
0.01
0.1
1
10
100
1000
10000
t' (time)
Lead on short unstable orbit
Classical
Generic lead location

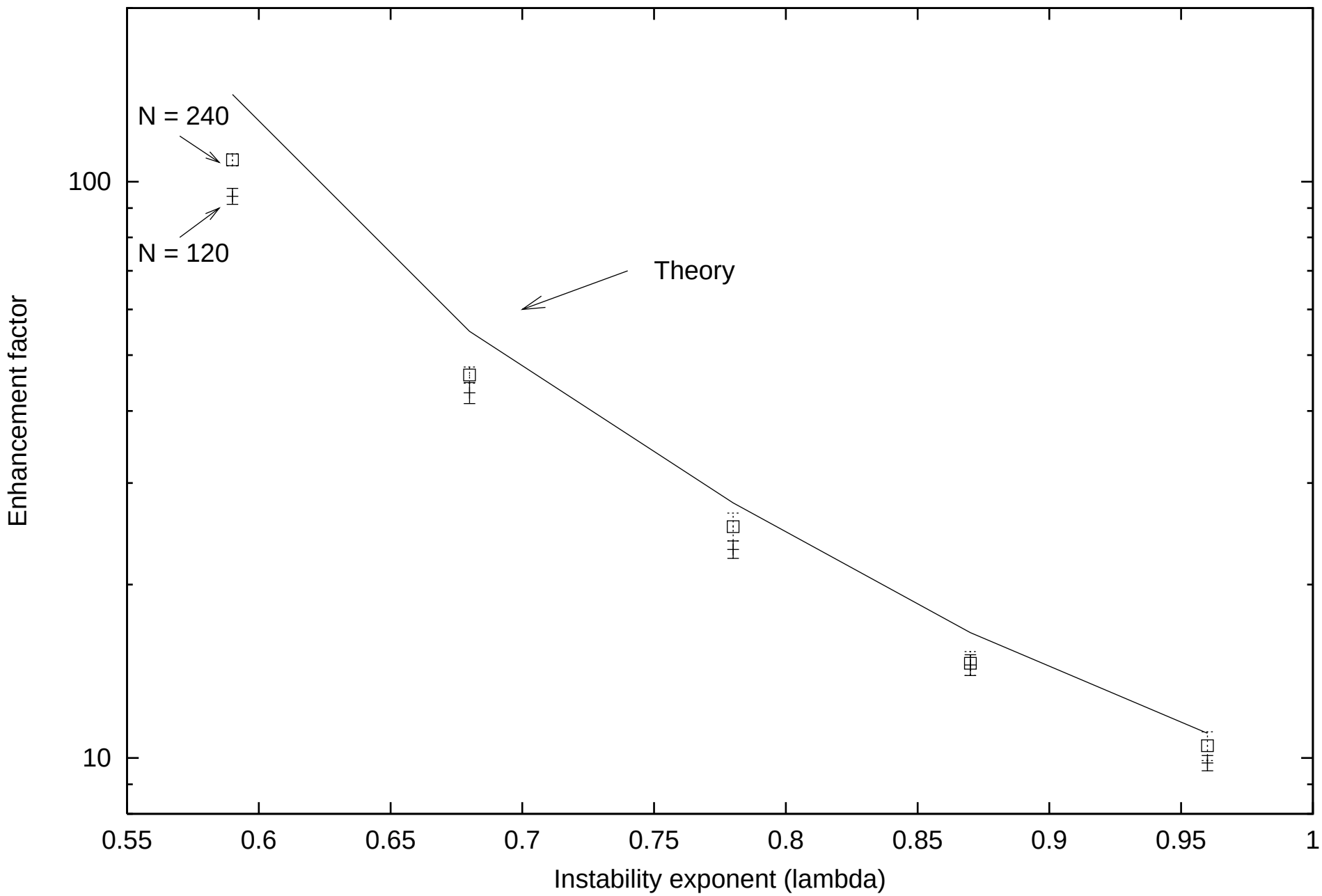
N = 240
N = 120
Theory
100
10
Enhancement factor
0.55
0.6
0.65
0.7
0.75
0.8
0.85
0.9
0.95
1
Instability exponent (lambda)

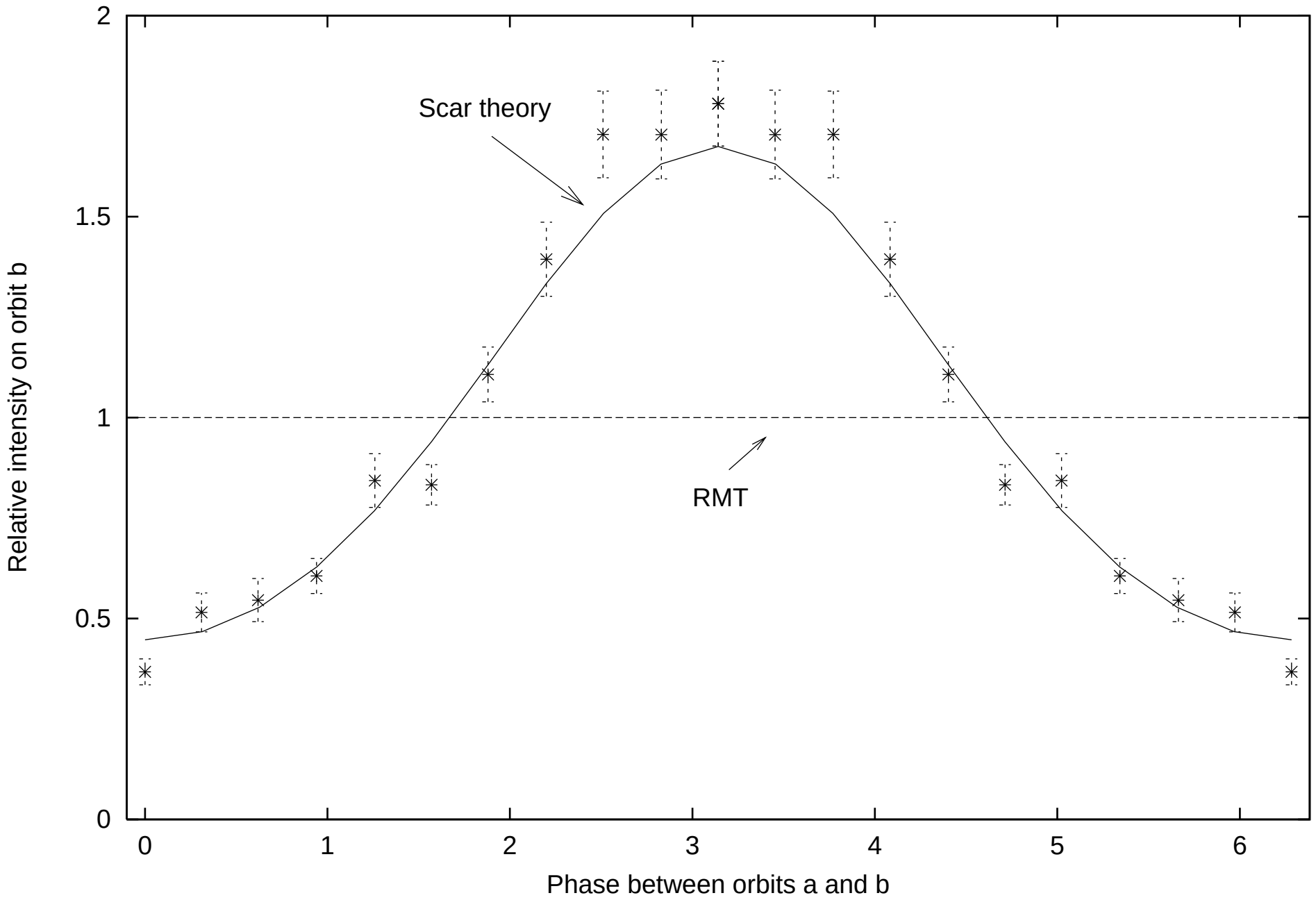
Scar theory
RMT
Relative intensity on orbit b
Phase between orbits a and b
0
0.5
1
1.5
2
0
1
2
3
4
5
6